Title
Magnetoelectric Devices and Multiscale Modeling

Author
Hsiao, Yu-Ching

Publication Date
2022

UNIVERSITY OF CALIFORNIA

Los Angeles

Magnetoelectric Devices and Multiscale Modeling

A dissertation submitted in partial satisfaction of the

requirements for the degree Doctor of Philosophy

in Mechanical Engineering

by

Yu-Ching Hsiao

2022

ABSTRACT OF THE DISSERTATION

Magnetoelectric Devices and Multiscale Modeling

by

Yu-Ching Hsiao

Doctor of Philosophy in Mechanical Engineering

University of California, Los Angeles, 2022

Professor Christopher S. Lynch, Co-Chair

Professor Gregory P. Carman, Co-Chair

Multiferroic materials facilitate the novel development of magnetic devices. Extensive effort has been devoted to the multiferroic field to overcome the scaling limitations in past decades. Likewise, this work focused on increasing energy efficiency and density through the applications, development, and fundamental studies of multiferroics. Application such as cell sorting was proposed to resolve the cell aggregation problem of the conventional method through the permanent magnet. Co/Ni multilayers exhibiting perpendicular magnetic anisotropy (PMA) were designed, fabricated, and tested for the cell sorting application. The cell capture method demonstrates a way towards compact lab-on-a-chip devices for more precise cell sorting control. In this study, we observed an inhomogeneous response across these Co/Ni microdevices. This drove us to investigate the roughness and magnetoelectric effects on the magnetic behavior across the microdevices. The homogenous response is critical to reliable strain-mediated multiferroic devices. We fabricated Co/Ni microdisks on the $[Pb(Mg_{1/3}Nb_{2/3})O_3]_{0.7}$–$[PbTiO_3]_{0.3}$ (PMN-30PT) substrate, and characterized them using magneto-optic Kerr effect (MOKE) method to obtain the coercivity of each individual microdisks. The results were used to study the dependence on roughness and electric field-induced strain in the substrate. This study aimed to assist the reliable design of strain-mediated PMA based devices. Lastly, an atomic model was developed to understand static and dynamic magnetic behaviors using a multiscale modeling approach. Two Co adatoms on a Cu(100) substrate were modeled by incorporating the atomic displacement effects. The parameters used in the model were extracted from the density functional theory (DFT) calculation. Ferromagnetic to antiferromagnetic transition, and in-plane to out-of-plane switching were observed with changes made to the atomic displacement and applied external field. Additionally, the tunability of the resonance frequency of the two-adatom system was demonstrated with the magneto-displacement effect. The outcome shows that the atomic level devices are promising for the potential application of quantum computing and storage devices. When viewed together, the studies provide the foundational tools to develop next-generation multiferroic devices.

The dissertation of Yu-Ching Hsiao is approved.

Kang L. Wang

Robert N. Candler

Gregory P. Carman, Committee Co-Chair

Christopher S. Lynch, Committee Co-Chair

University of California, Los Angeles

2022

To my parents, Lieh-Tsung Hsiao, Su-Mei Cheng,

and my sister, Yu-Jung Hsiao

Table of Contents

List of Figures

ACKNOWLEDGEMENTS

Never did I expect the whole Ph.D. journey to be so challenging and exciting. What I have valued the most in the journey is the lovely people around me. I would like to thank my advisor Professor Lynch. He has been very supportive and has always encouraged me to explore the fields I am interested in. He always puts himself in the student's place and figures out what would benefit students in the long term. I am very thankful to have had him as my advisor. He has helped me grow academically and personally. I also would like to thank Dr. Carman. He has always encouraged me to think out of the box and realize my full potential. I also thank my Ph.D. committee Professor Kang Wang and Professor Rob Candler. I always feel motivated after inspirational conversations with them.

Throughout my Ph.D. studies, I have been very lucky to have mentors guiding me along the way. In 2018, I worked with Dr. Dan Gopman at NIST for a month. I learned how to use instruments and analyze data from him. We had lunch every day and talked about a wide range of topics. It was a great time. After I came back to the west coast, we stayed in touch and continued working together. He has always generously offered help whenever I needed it, and I appreciate it. I would like to thank Dr. Oleg Udalov for providing guidance on the atomic model project. He has given brilliant advice when I got stuck. I have really enjoyed discussions with Oleg. I also would like to thank Dr. Farzad Mahfouzi for supporting me and patiently explained to me the DFT calculations for the atomic project.

To my wonderful lab mates from the labs of Dr. Lynch and Dr. Carman, they truly make my everyday work fun. We could discuss research seriously but also joked around. We always thought about how to help each other and this contributes to a wonderful lab vibe. Xu Li was the first person I met when Professor Lynch introduced me to his lab. She is one of the kindest people I have met. She patiently shared her lab experiences with me and helped me with the background preparation of magnetics when I had just joined the lab. I also want to thank Peng, QC, Cai Chen for advice and discussions. I enjoyed weekends when we treated ourselves to authentic delicious Asian food after hiking. Next, I have to thank Auni, Andres, Devin, and Tony all four together, because they are bonded together like a happy family. Auni is such a sweet person who always offers to help and shows caring. She has brought people together and created a warm environment in the lab. Andres always saved me when I was drowning, i.e. fabrication, writing, and presenting. I grew independently with his help. With Devin, we talked about anything and everything. I got to know American cultures and some trivia from boundless conversation with him. Tony is very eloquent and he could give a speech on almost every topic. His suggestions were always very helpful and succinct.

In 2019, most of the senior people in the lab graduated, and some more lovely people joined the lab. I enjoyed having fun times with Emily, Paymon, and Michael G. We went to Barney’s, grabbed boba, and celebrated birthdays and holidays together. I also would like to thank Mohan, John, Michael S., Matthew, Victor, Rouda, and Jesse. We discussed research and also played spikeball together. You all have made my lab life an absolute joy. I would like to thank people outside the lab who have supported me through my Ph.D. studies. I would like to thank Carol, Wenzhong, and TK for all the delicious food parties, and Leah and Ha for all the relaxing walks and brunches. I appreciate Steve, Gena, Yen Ru, and Albert’s support on everything from my first year at UCLA. I would like to thank my friend Xu Liu. We have cheered each other up when feeling down, and have shared joy and inspired changes in each other. I would love to thank Lilian and Dr. Martin for guiding and supporting me through the most difficult times. Also, to my friends in Taiwan and Sweden, thank you all for being friends with me despite how far apart we are.

Most importantly, to my family, it is difficult to express my gratitude to them with only words. To my father Lieh-Tsung Hsiao, he has always been supporting me to pursue my dreams. From Taiwan to Sweden, and to the U.S., his trust in me and my decisions through my life has been an important foundation for me. He is the anchor of my whole family. To my mom, Su-Mei Cheng, her attitude and wisdom has been inspiring me to think more optimistically. She cares less about my achievements but more about whether I am truly happy or not. To my sister, Yu-Jung Hsiao, we are very independent individuals but also codependent sisters. She moved from England to Taiwan. Although we live in different time zones, we still share little things in daily life. I have always called her when I had breakdowns alone by myself late at night. Chatting with her gave me a sense of peace and courage to move on.

I am a blessed person to be surrounded by many people who love me, and I love them too.

Yu-Ching Hsiao

VITA

Education

2022 M.S., Mechanical Engineering

University of California, Los Angeles, USA

2013 M.S., Materials Physics and Nanotechnology

Linköping University, Sweden

2011 B.S., Physics and Electrical Engineering

National Tsing-Hua University, Taiwan

Employment History

2020 Process Engineer Intern

Maxim Integrated, USA

2014-2015 Research Assistant

Institute of Physics, Academia Sinica, Taiwan

Publications

- **Hsiao, Yu-Ching**, et al. “Capturing magnetic bead-based arrays using perpendicular magnetic anisotropy.” *Applied physics letters* 115.8 (2019): 082402.

- Drobitch, J. L., **Hsiao, Yu-Ching**, et al. “Effect of CoFe dusting layer and annealing on the magnetic properties of sputtered Ta/W/CoFeB/CoFe/MgO layer structures.” *Journal of physics D: Applied physics* 53.10 (2019): 105001.

- **Hsiao, Yu-Ching**, et al. “Effect of Interfacial and Edge Roughness on Magnetoelectric Control of Co/Ni Microdisks on PMN-PT(011).” *Scientific Reports* (2022) Accepted.
- **Hsiao, Yu-Ching**, et al. “Mechanical Control on Atomic Spin Model.” (2022) Under preparation.

Presentations

- **Hsiao, Yu-Ching**, et al. “Capturing Magnetic Bead-based Arrays Using Perpendicular Magnetic Anisotropy (PMA).” Oral Presentation at Joint-Intermag conference, Washington DC (2019).
- **Hsiao, Yu-Ching**, et al. “Strain Effect in Atomic Spin Model.” Oral Presentation at MMM conference, Las Vegas (2019).
- **Hsiao, Yu-Ching**, et al. “Strain-assisted Co/Ni Multilayer Structure for Memory Device Application.” Poster Presentation at SPIE conference, Denver (2019).
- **Hsiao, Yu-Ching**, et al. “Multilayer Co/Ni Memory Device with Perpendicular Magnetic Anisotropy (PMA) Effect.” Poster Presentation at IMRC conference, Mexico (2018).

Chapter 1. Introduction

1.1 Motivation

a. Strain-mediated device with perpendicular magnetic anisotropy (PMA)

Strain-mediated approaches utilizing ferromagnetic materials and ferroelectric substrates have been demonstrated to be one of the most energy efficient methods for the control of magnetism [1][2]. In these heterostructures, electric field induced strain generated in the ferroelectric substrate is transmitted to a ferromagnetic thin film. The energy landscape of the ferromagnetic film is altered due to magnetoelastic coupling, causing reorientation of the magnetization.

D.P Gopman demonstrated strain-assisted magnetic reversal in a Co/Ni magnetic film on a ferroelectric PMN-PT substrate. He proposed its potential for applications in strain-mediated memory storage devices [3]. Co/Ni multilayers have been widely studied due to their strong perpendicular magnetic anisotropy (PMA). PMA describes the case where the easy axis of magnetization is perpendicular to the plane of the heterostructure or film. Strong PMA provides the advantage of high thermal stability. In patterned thin film structures, PMA results in relatively uniform magnetization compared to in-plane anisotropy, especially at the edges of the patterned microstructures [4].

Inspired by Gopman's work, a magnetic bead capture device using patterned Co/Ni heterostructures was developed, (discussed in Chapter 2). This work demonstrates voltage-assisted magnetization reversal with a moderate magnetic bias field, resulting in a high PMA Co/Ni multilayered film coupled with a ferroelectric substrate being a promising candidate for voltage-assisted spintronic devices. In Chapter 3, the effect of interfacial and edge roughness on magnetoelectric control of Co/Ni microdisks is investigated. The results provide guidance to future design of strain modulated PMA based devices.

b. Atomic model with multiscale approach

The design of magnetic devices at small length scales requires phenomenological and computational schemes that bridge different length scales. A multiscale modeling approach was used that integrates the methods and bridges the gap between different scales to predict material behavior. The materials multiscale simulations range from the quantum scale to mesoscale the length scale ranges, and from picometer to micrometer. Several methods are very well-developed at different scales[5]. For example, density functional theory (DFT) is one of the most-utilized methods at the quantum level. Material properties can be obtained using DFT methods in terms of electron densities. The quantum scale is limited to a small number of atoms due to computational constraints. On the other hand, finite element methods are often used for continuum-level systems to predict material behavior at mesoscales. At the research center, the Translational Applications of Nanoscale Multiferroic Systems (TANMS), finite element methods and DFT have been routinely applied to investigate multiferroic systems. In this work atomic scale simulations are used to bridge between the quantum and mesoscales. Small scale devices (10 to 100 nm) are being investigated, and atomic models are beginning to provide enhanced capability to study device behavior across length scales.

Our phenomenological model at the atomic scale uses material constants calculated by the DFT calculations. The atomic scale model is then employed to investigate statics and dynamics of atomic magnetic moments. The combination of models at different scales significantly reduces the computational cost. Without restarting each calculation from the quantum scale, the atomic model using the DFT parameters as input to enable modeling of magnetic system dynamics. The developed atomic model incorporated with the magnetostrictive effect is discussed in Chapter 4.

1.2 Background

a. Characterization of PMA heterostructure — magneto-optical Kerr effect (MOKE)

Magneto-optical Kerr effect (MOKE) is a technique used to characterize the change in polarized light reflected from magnetized specimens [6]. There are three types of measurement based on polarization states in MOKE, as illustrated in Figure 1.1. (1) Polar MOKE: the magnetization direction is perpendicular to the surface. (2) longitudinal MOKE: the magnetization is parallel to the surface and the plane of incident and reflected lights. (3) Transverse MOKE: the magnetization is perpendicular to the incidence plane, and parallel to the surface. MOKE results are generally demonstrated as a hysteresis loop with the Kerr signal plotted against the external magnetic field. The orientation of magnetization determines the type of MOKE utilized for characterization.

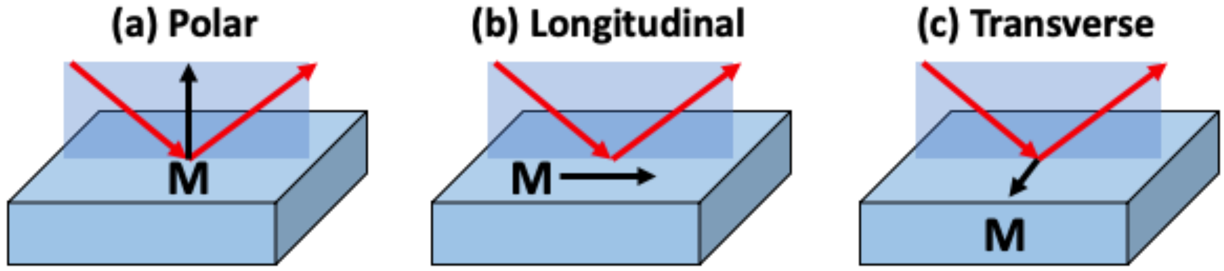

Figure 1.1 Schemes of three types of MOKE measurements. (a) Polar MOKE (b) Longitudinal MOKE (c) Transverse MOKE.

One of the key magnetic properties, the coercive field, can be obtained in the MOKE hysteresis loop. Coercivity describes the required external field to complete switching and saturate the magnetization. In our work, Co/Ni PMA heterostructures are characterized using polar MOKE to monitor both changes in the out-of-plane magnetization and coercivity.

Atomic spin simulations were initially implemented based on density functional theory (DFT) in 1995 [7], [8]. Theories of magnetic Hamiltonians were widely studied in the beginning of 2000s [9]. To reduce the computational cost, DFT calculations were subsequently combined with classical Hamiltonians. The parameters extracted from DFT results or experiments can be used in Hamiltonian models to speed up calculations. Based on the multiscale framework, several packaged codes were developed such as ASD[10], SPIRIT[11], and VAMPIRE[12].

Atomic simulations (AS) provides the atomistic description of magnetization dynamics. Figure 1.2 shows the difference between atomic spin and macrospin in AS and micromagnetics. In the AS system, each small spin is associated with each atomic site; whereas in micromagnetics, instead of each individual atomic spins, macrospin represents the total spins in the sublattice.

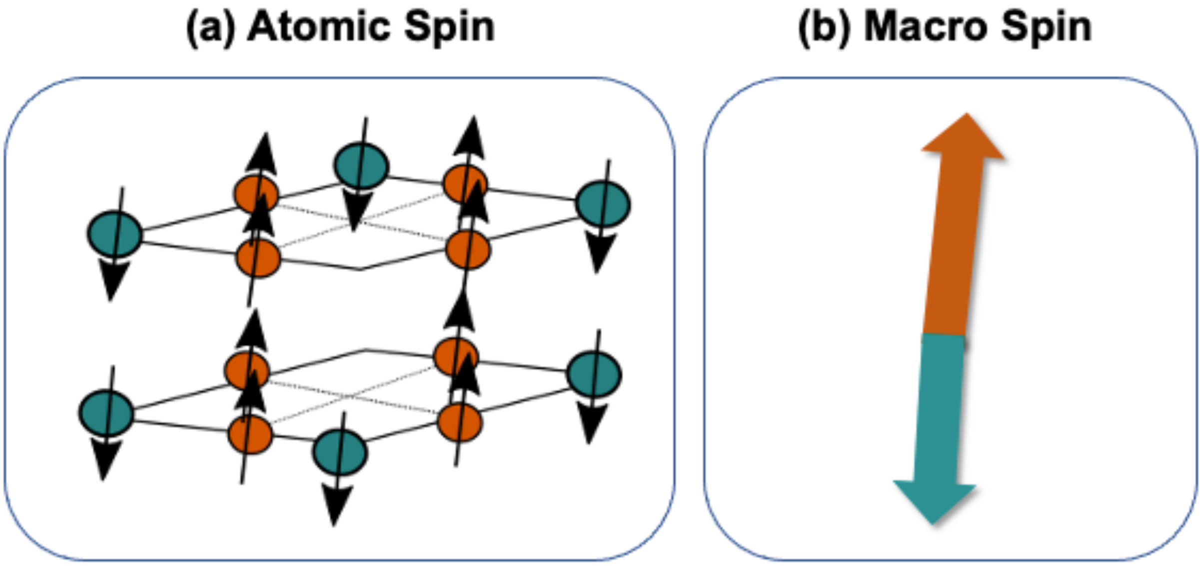

Figure 1.2 The sketch of magnetic spins at different scales. (a) atomic spin (b) macro spin. The figure is adapted from the paper written by Atxitia et al. [13]

Atomic simulation is governed by the LLG equation with an atomic spin $\vec{M}$ on each discrete atomic sites[14], whereas the magnetization in micromagnetics is a continuum scale volume average effect.

$$\frac{\partial \vec{M}}{\partial t} = \gamma \vec{M} \times \overrightarrow{H_{eff}} - \alpha \vec{M} \times \frac{\partial \vec{M}}{\partial t} \tag{1.1}$$

where γ is gyromagnetic ratio; α is the damping coefficient; $\overrightarrow{H_{eff}}$ is the effective field.

The effective field is obtained by differentiating the Hamiltonian ($\mathcal{H}$) with respect to magnetization

$$\overrightarrow{H_{eff}} = -\frac{1}{\mu_0 M_s} \frac{\partial \mathcal{H}}{\partial \vec{M}} \tag{1.2}$$

where μ_0 denotes permeability of the free space; M_s is saturation magnetization.

The Hamiltonian comprises different terms

$$\mathcal{H} = \mathcal{H}_{ex} + \mathcal{H}_{an} + \mathcal{H}_{dd} + \mathcal{H}_{ext} + \mathcal{H}_{el} \tag{2.13}$$

(1) $\mathcal{H}_{ex}$ is the interatomic exchange Hamiltonian.

(2) $\mathcal{H}_{an}$ is the anisotropy energy term.

(3) $\mathcal{H}_{dd}$ is long range dipole-dipole term. The interaction between dipoles are either attraction or repulsions.

(4) $\mathcal{H}_{ext}$ is the external field energy term, also known as Zeeman energy

(5) $\mathcal{H}_{el}$ is the elastic energy term, mechanical energy in atomic system.

The exchange energy shows distinct differences in micromagnetic and atomic systems based on the continuum and discrete magnetizations, respectively. In the micromagnetic system, exchange energy (E_{ex}) is approximated by taking the gradient of continuum magnetization. However, the atomic model considers the interactions between each spins.

Micromagnetic:
$$E_{ex} = A_{ex} \left(\nabla \frac{\boldsymbol{M}}{M_s}\right)^2 \tag{1.3}$$

Atomistic:
$$\mathcal{H}_{ex} = -\frac{1}{2}\sum_{i \neq j} J_{ij}\, \boldsymbol{m}_i \boldsymbol{m}_j \tag{1.4}$$

where A_{ex} denotes exchange stiffness constant; i, j are atomic spin indices; J_{ij} the strength of exchange interaction.

The expressions for each of the energy term are discussed in Chapter 4.

Chapter 2. Capturing Magnetic Bead-based Arrays Using Perpendicular Magnetic Anisotropy (PMA)

2.1 Introduction

Magnetic bead-based methods have facilitated many biomedical applications such as cell sorting and separation[15]. The cell separation method was first developed by Miltenyi et al [16]. The cell labeled with magnetic beads suspended in a fluid can be separated from the other unlabeled ones using magnets. Conventionally, target cells are separated from suspension using external magnetic field from hard permanent magnets or electromagnetic coils. However, the large external magnetic field leads cells to aggregate to one location in the reaction chamber leaving limited space for imaging and analysis to quantify different analytes simultaneously[17]. External magnetic field-based microfluidic systems cannot currently assemble micromagnetic beads uniformly in arrays to allow detection and analysis. Precise localization of magnetic beads at the microscale is needed for precise cell localization.

This chapter demonstrates magnetic bead assembly in a uniform array using the magnetic force produced by disk shaped heterostructures displaying perpendicular magnetic anisotropy (PMA)[18]. PMA describes the case where the easy axis of magnetization is perpendicular to the plane of the heterostructure or film. This effect occurs in certain ultrathin film systems and at the interface of multilayers[19][20]. Co/Ni multilayers were selected for their large PMA compared to other Co-containing multilayers such as Co/Ag and Co/Au[21][22]. Anisotropy energy and saturation magnetization (M_s) can be adjusted by modification of the relative thickness of the layers[3]. In comparison to other methods[23]–[28], the PMA assisted capture method does not require external fields or other energy to be supplied, simplifying its use. This has the potential to enable lab-on-a-chip cell manipulation devices[29][30].

In this study, disk arrays with PMA were designed, fabricated, and demonstrated to be capable of capturing micron scale magnetic beads suspended in a fluid [31]. In the next section, the model used to simulate the capture force arising from a magnetic gradient generated by Co/Ni disk is described. Heterostructures with PMA generate a magnetic field gradient in their vicinity that attracts the magnetic beads. The PMA heterostructures were designed using the simulation results, followed by fabrication and testing in a microfluidic platform. The outcome shows that the majority of beads are trapped on the disk perimeter, which agrees with the modeling results.

2.2 The model

A numerical model was used to determine the distribution of bead trapping force produced by a Co/Ni disk as well as changes in bead capture force due to varying the M_s value of the Co/Ni disk [20][21][34]. A finite element approach was used to simulate the magnetic field distribution around the Co/Ni disk and its interactions with a magnetic bead. The thickness of Co/Ni was set at 4 nm and uniform out-of-plane magnetization with magnitude M_s was initialized within the disk resulting in a magnetic field exterior to the disk. The out-of-plane initialization of magnetization duplicates the PMA effect. The magnetic force components on the bead were calculated at different spatial positions within this field using the finite element simulations together with Eqs. (2.1)-(2.4). The calculated magnetic field distribution was used with post processing to determine the bead capture force.

The capture force was calculated using Eq. (2.1):

$$\boldsymbol{F_{bead}} = -\nabla U \tag{2.1}$$

where F_{bead} is the capture force of the bead expressed as the negative gradiet of the potential energy U.

The total magnetic potential energy, U, is an integration of magnetic energy density (u) over the bead volume using Eq. (2.2).

$$U = \iiint_V u \, dV \tag{2.2}$$

The energy density was determined using Eq. (2.3):

$$u = -\boldsymbol{M} \cdot \boldsymbol{B} \tag{2.3}$$

where M is the induced magnetization in the magnetic bead and B is the magnetic flux generated in the bead by Co/Ni disk. The relation between B and M is expressed by Eq. (2.4):

$$\boldsymbol{B} = \mu_0 \left(1 + \frac{1}{\mathcal{X}_m}\right) \boldsymbol{M} \tag{2.4}$$

where μ_0 is the vacuum permeability; $\mathcal{X}_m$ is magnetic susceptibility [23][24][37]. From Eqs. (2.1-2.4), the capture force is related to the bead volume and magnetic flux generated from the Co/Ni disk, proportional to M_s^2 of Co/Ni disk.

For the simulations, the bead position was varied from coincident with the disk center to -3 µm horizontal displacement in 500 nm increments. Since the magnetic force is spatially symmetric, calculations were only performed for one half of the disk. The net force was calculated for a series of bead diameters and M_s values of a prospective Co/Ni disk. Specifically, five values of M_s, {600, 700, 800, 900, 1000} kA/m, were selected. These choices were made because they span the possible range of expected M_s values for Co/Ni multilayers. The bulk M_s values of Co and Ni are 1400 kA/m and 490 kA/m [38][39], respectively and can be achieved by varying the relative layer thickness. Each M_s value was tested with four different bead diameters of {0.2, 0.4, 0.6, 0.8} μm. These bead diameters were chosen because smaller magnetic beads provide higher spatial resolution when imaging the distribution of the magnetic beads in the testing section. A 4 μm diameter Co/Ni disk was used in all simulations.

2.3 Fabrication

Simulation results indicate that high M_s yields larger trapping force on the bead. This can be achieved via a high Co to Ni ratio. However, overly large Co to Ni ratio risks losing PMA [3][40][41]. A Co (0.2 nm)/Ni (0.4 nm) structure was selected for its relatively high M_s while maintaining stable perpendicular magnetization. This structure was produced on a 0.5 mm thick single crystalline Si (001) substrate by e-beam evaporation [42][43] at room temperature with a base pressure of $2\text{x}10^{-6}$ torr. Four repeated Co (0.2 nm)/Ni (0.4 nm) layers were grown on top of a Pt (3 nm) buffer layer and a Ti (2 nm) adhesion layer. Pt was chosen as the seed layer because it has been experimentally demonstrated to enhance the PMA in Co/Ni multilayers [44]. Ti was chosen to improve adhesion of Pt to the substrate. For symmetry, an extra Co layer (0.2 nm) was deposited on top of Co/Ni multilayers. The entire structure was then capped by a Pt (3 nm) layer to prevent metal oxidation. Disks with 4 μm – 7 μm diameters and 12 μm separation between the centers of disks were patterned by a lift-off method using photoresist nLof2020. To benchmark the relevant M_s of this heterostructure, a full film sample was characterized by Superconducting Quantum Interference Device (SQUID) in DC mode to confirm the presence of an out-of-plane easy axis consistent with PMA.

2.4 Trapping of fluorescent beads

The structure was next tested for trapping fluorescent beads using a microchannel. A microfluidic device was integrated with the Co/Ni disks and fluorescent magnetic beads were passed in a PDMS channel and imaged with a fluorescent microscope to observe the magnetic bead capture events. The PDMS microchannels were fabricated with standard soft-photolithography. PDMS (Sylgard 184, Dow Corning, Midland, MI, USA) was mixed with a curing agent at a 10:1 weight ratio. The mixture was poured onto the master wafer and degassed for one hour to remove air bubbles then cured at 100°C overnight. Microchannel devices were cut out and aligned on the surface of Co/Ni multilayer micropattern on silicon to test magnetic bead-based capture. Magnetic beads with diameter of 0.4 µm – 2.8 µm (Spherotech, Libertyville, IL) were suspended in distilled water. The magnetic microbead surface was functionalized with fluorescent dye to visualize localization of beads on Co/Ni multilayer microdisks.

The specimens were viewed using an inverted microscope Nikon Ti-U (Nikon, Melville, NY) illuminated by a mercury arc lamp with 10× and 40× objectives. Fluorescent micro and nanobeads captured on a magnetic array were imaged with a CCD Coolsnap HQ2 camera (Roper Scientific, Evry, France). Images were processed by NIS Elements software (NIS-Elements Package Ver. 4.00, Nikon) then analyzed using an in-house MATLAB code to overlay fluorescent images of beads distribution on the Co/Ni multilayer micropattern.

2.5 Results

a. Simulated capture force

The simulated capture force vs. bead location profile for one combination of parameters is presented in Figure 2.1(a). This shows the results for a Co/Ni disk with M_s of 800 (kA/m) and bead diameter of 0.8 (µm). The capture force rises as the bead is moved from the left side towards the center of the disk and reaches a peak value at the disk edge (i.e. x = -2 µm). The force falls as the bead location is moved further to the right and approaches the center of Co/Ni disk. The maximum net force occurs at the disk edge where the largest magnetic flux gradient is from the disk is generated.

The maximum force as a function of bead diameter at various M_s values is illustrated in Figure 2.1(b). The plot shows that maximum force does not change significantly with the bead diameter, which provides flexibility in choosing the nanomagnetic bead size. This can be explained by recognizing that the magnetic field from the Co/Ni disk is localized to the edge causing a magnetization gradient in the bead. Consequently, the magnetized volume does not significantly change even with increasing bead diameter. In contrast, the capture forces show high dependence on the value of M_s, which proves the magnetic flux is proportional to M_s of the Co/Ni disk. For example, the maximum force increases ~ 2 times when increasing the M_s value from 700 kA/m to 1000 kA/m. The advantage of using a multilayer structure is that the relative thickness between Co and Ni films is readily tunable. Hence, it is experimentally possible to modify the maximum capture force by tuning the M_s of the Co/Ni multilayers.

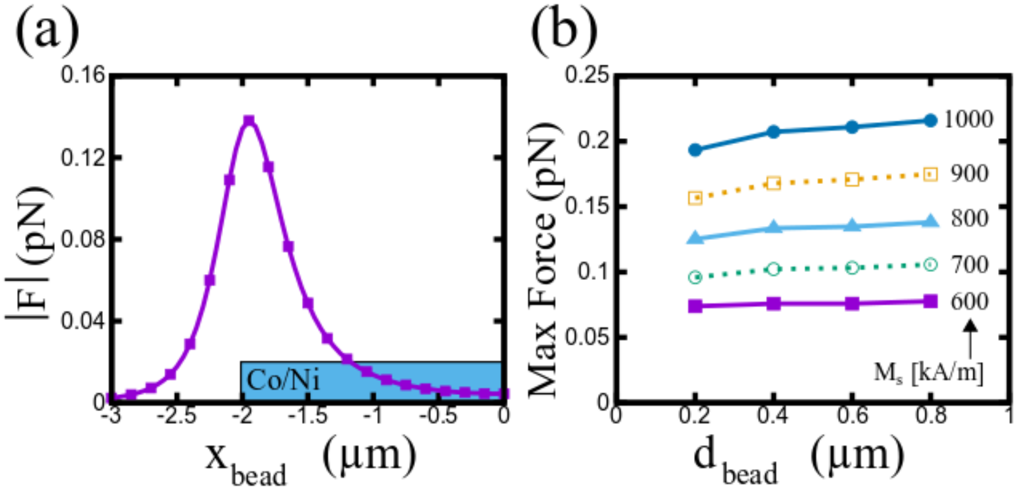

Figure 2.1 (a) Force on a magnetic bead (0.8 μm diameter) when placed at different locations. The blue box indicates the half side of Co/Ni disk. (b) Maximum force determined from different M_s

values of Co/Ni disk as a function of each bead diameter. The maximum capture forces for (b) were extracted from the peak value of a corresponding force profile similar to the one shown in (a).

b. Hysteresis characterization of the PMA heterostructure

The presence of an out-of-plane easy axis consistent with PMA is confirmed in the hysteresis loop characterized by SQUID shown in Figure 2.2. The out-of-plane (OOP) curve has much lower saturation field and higher magnetic remanence than the in-plane (IP) curve. Furthermore, experimental values for OOP M_s (870 kA/m) and IP (860 kA/m) are consistent with the theoretical value 840 kA/m, which was obtained from the Co/Ni thickness ratio (1 : 1.6) by the rule of mixtures. The bulk M_s values of Co and Ni are 1400 kA/m and 490 kA/m [38][39], respectively. This confirms that the desired M_s was obtained by growing a film with the relevant Co to Ni thickness ratio.

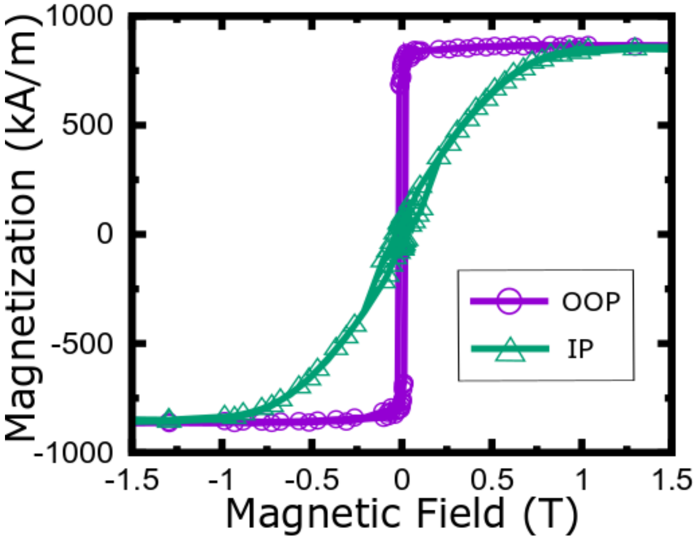

Figure 2.2 Magnetization versus applied field hysteresis loop for a full film Co (0.2 nm)/Ni (0.4 nm) heterostructure under in-plane (IP) and out-of-plane (OOP) applied fields.

c. Fluorescent bead captured by Co/Ni disks

The disk array is shown in Figure 2.3(a). Magnetic beads were localized on the Co/Ni micro-pattern array as shown in Figure 2.3(b). To provide further evidence to support bead-based capture via PMA, the disk arrays were partially covered with a PDMS layer of 1 mm thickness prior to introducing the magnetic beads in suspension. The beads were not captured by PDMS covered disks, Figure 2.3(c).

The PMA field capture and localization were characterized by tracking magnetic bead binding sites on the surface of Co/Ni disks. Micromagnetic beads (diameter = 2.8 μm) labeled with red fluorescent dye in fluid were introduced to Co/Ni disks (diameter = 7 μm). Magnetic binding locations were observed on the edges of the Co/Ni disks (Figure 2.3(d)). Specifically, micromagnetic beads were equally distributed and localized at different angles (θ) from the center of each disk. This indicates a large magnetic field gradient associated with the magnetization field produced on the perimeter of Co/Ni disks as suggested by the simulations.

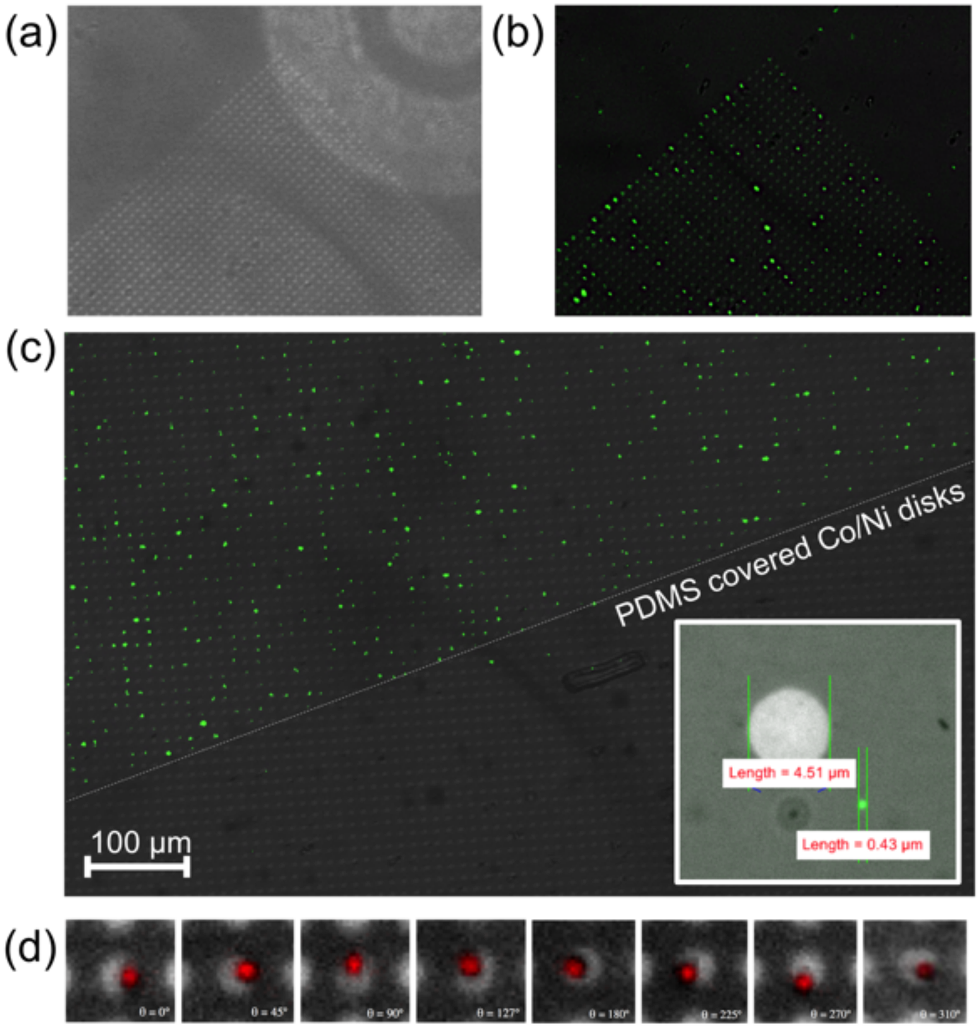

Figure 2.3 Co/Ni multilayer disks (diameter = 4.5 μm) with PMA demonstrate high capture rate of magnetic beads labeled with green fluorescence (diameter = 0.4 μm). (a) Bright field image of Co/Ni multilayer disks before passing fluorescent magnetic beads. (b) Overlay of bright field and fluorescent images of magnetic beads on the Co/Ni disk array demonstrates localized capture. (c) Partially covered substrate with PDMS layer shows selective binding and localization of fluid-born beads on Co/Ni multilayer disks. (d) The location of magnetic bead-binding events at different angle (θ) with the polar coordinate system chosen at (1,0) on the circular surface of the Co/Ni micro-disks.

Smaller magnetic beads were used to increase the spatial resolution when imaging magnetic beads. These fluorescent nanomagnetic particles (diameter = 400 nm-500 nm) were captured on the previously tested Co/Ni disks (diameter = 7 μm) (Figure 2.4(a)). Quantitative measurements of nanomagnetic bead localization were made by image analysis of the fluorescent intensity (grayscale) around the Co/Ni disks. An overlay image of the disks was generated, where pixels with larger intensity corresponds to the location of nanomagentic beads (Figure 2.4 (b)). The normalized image intensity map confirms that the most effective magnetic trapping region coincides with the region of maximal magnetic field gradient at the perimeter of Co/Ni disks (Figure 2.4 (c)).

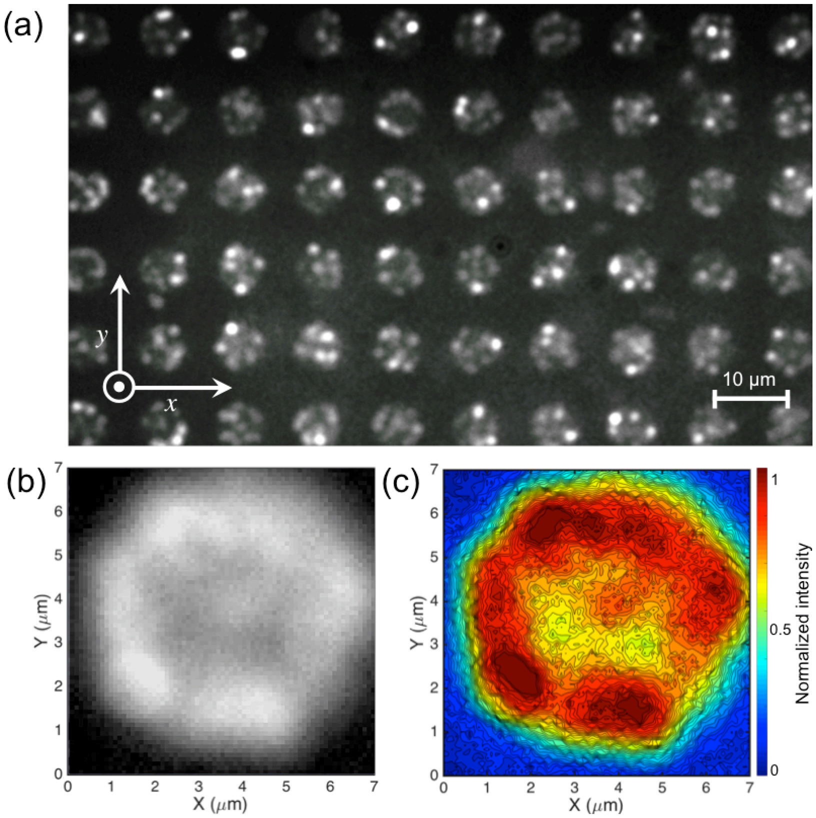

Figure 2.4 Quantitative image analysis of nanomagnetic beads distribution on the surface of Co/Ni disks. (a) Fluorescent microscope image of nanomagnetic capture and build-up on 7 μm Co/Ni

disks. (b) Fluorescent intensity of an image overlay of Co/Ni disks (c) Normalized intensity map of the image overlay show high magnetic trapping region on the perimeter of Co/Ni disks.

2.6 Summary

Multilayered Co/Ni disk arrays exhibiting PMA were designed, fabricated and demonstrated to capture magnetic beads. Finite element simulations indicate that different M_s values, which can be modified by varying the relative Co/Ni thickness ratio, significantly change the magnetic capture forces. Based on the modeling results, a Co (0.2 nm)/Ni (0.4 nm) multilayered structure was selected due to its OOP easy axis and relatively large PMA. Patterned Co/Ni disks were tested in a suspension of fluorescent magnetic beads in fluid, showing that the perimeter of disks trapped most of the magnetic beads. This observation agreed with the modeling results that the maximum capture force occurs at the edge of the disk. By eliminating the need for an externally applied field, this approach to magnetic bead capture provides a promising pathway towards compact lab-on-a-chip devices for more precise cell manipulation.

Chapter 3. Effect of Interfacial and Edge Roughness on Magnetoelectric Control of Co/Ni Microdisks on PMN-PT(011)

3.1 Introduction

Strain-mediated magnetoelectric (ME) heterostructures consisting of ferromagnetic (FM) and ferroelectric (FE) constituent layers are being explored as an advantageous device structure for local control of polarization, strain and magnetization at micron and sub-micron length scales[45]–[47]. Small-scale magnetic structures have certain applications, such as cell-sorting[30], cancer-cell destruction[48], bacteria isolation[49], and microsurgery[50], that would realize advances in overall size, energy efficiency and precision by migrating from traditional coil-based techniques to strain-modulated magnetization in such coupled FM-FE heterostructures[51]. Uniform magnetic behavior among these ME heterostructures is critical to the large-scale manufacturability of reliable strain-mediated devices [52], [53].

In ME heterostructures, the magnetization of an overlaid thin film can be manipulated using strain from a FE substrate via magneto-elastic coupling. Single-crystal, relaxor ferroelectric (011)-oriented $[Pb(Mg_{1/3}Nb_{2/3})O_3]_{1-x}$–$[PbTiO_3]_x$ (PMN-PT) have been investigated in prior studies for their in-plane anisotropic strain, i.e. compressive strain in the [100] direction and tensile strain along the [01-1] direction. One recent study pointed to micrometer-scale variation in the strain generated from the FE PMN-PT substrate limiting the degree of uniform remagnetization behavior in an overlaid FM[54]. However, this inhomogeneous strain distribution may not be the only contribution to non-uniform behavior. Other possible contributors include interfacial and edge roughness[55]–[59]. Prototype ME heterostructures were desgined and fabricated to better quantify these alternative contributors to non-uniform magnetization reversal behavior. Co/Ni microdisk heterostructures were patterned on PMN-30PT (011) and Si substrates to evaluate the magnetic coercive field and its variation across substrates and under strains from applied electric fields to the FE susbtrate.

Co/Ni multilayers exhibit strong perpendicular magnetic anisotropy (PMA)[3], [60], [61] that arises from the surfaces and interfaces of the ultrathin Co and Ni layers, with each alternating layer spanning less than 1 nm[18]. As interfacial effects dominate the magnetic anisotropy energy in Co/Ni, the magneto-elastic coupling in Co/Ni is also predominantly originating from surfaces and interfaces. Co/Ni films on PMN-30PT substrates have been shown to display a larger interfacial magnetostriction than the volume contribution[62]. This work reported on in this chapter was designed to explore the distribution of magnetic behavior across arrays of Co/Ni microdisks on a given substrate and to clarify the relative contributions of surface roughness, strain, and processing-induced lateral inhomogeneity that arises in the fabrication process. The coercivity of each Co/Ni microdisk was measured using magneto-optical Kerr effect (MOKE) magnetometry. Atomic force microscopy (AFM) was used to characterize the surface roughness of the Co/Ni multilayers on PMN-30PT and Si substrates. Scanning electron microscopy (SEM) was used to investigate the lateral inhomogeneity of patterned Co/Ni microdisks. The coercive field distribution was measured in an unstrained (zero electric field) Co/Ni microdisk array grown on PMN-30PT and compared to an identical array grown on a Si wafer to observe how the surface roughness affected the coercive field and the coercive field distribution across each array. The distribution of the coercive field among the heterostructures fabricated on the smooth Si is attributed to variations introduced in the fabrication process. The difference in the median coercive field between the smoother Si and rougher PMN-30PT specimens was attributed to surface roughness. Application of an electric field was used to study the influence of strain on the coercive field response in the magnetostrictive Co/Ni heterostructures.

3.2 Fabrication

Co/Ni microdisks were patterned on a 500 μm thick PMN-30PT substrate (011) single crystal (TRS Technologies, Inc., United States) as shown in Figure 3.1[63]. As depicted from the coordinate axes of Figure 3.1, the Co/Ni disks were deposited over the (011)-cut PMN-PT substrate, for which applied electric fields generate substantial expansion along the 01-1 axis with a more modest compression along the 100 axis. Electric-field induced strains are transferred to the films from the substrate and induce changes in the Co/Ni magnetization.

Electron beam evaporation was used for the deposition of Ti, Pt, Co, Ni, and Au at room temperature at a base pressure 3 x 10^{-4} Pa (2 x 10^{-6} Torr). The top and bottom surfaces of the PMN-30PT substrate were coated with 30 nm thick Au and Pt electrodes, respectively. The PMN-30PT with the electrodes was poled along the [011] direction with an electric field of 0.8 MV/m across the substrate for approximately one minute.

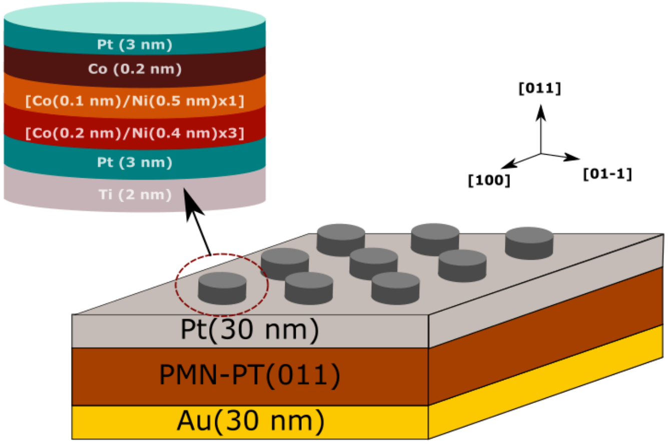

Figure 3.1. The structure of Co/Ni microdisks on the PMN-30PT substrate

The poled PMN-30PT substrate was cleaned using acetone, methanol, isopropanol, and a one-minute oxygen plasma treatment (80 W radio frequency power, 500 Pa, 50 ˚C) prior to the deposition of the Co/Ni films. A 2 nm thick Ti film was evaporated on the Pt electrode. Using a known recipe that consistently delivers high perpendicular magnetic anisotropy, we employ here three repeated Co(0.2 nm)/Ni(0.4 nm) bilayers followed by a Co(0.1 nm)/Ni(0.5 nm) bilayer were grown on the Pt(2 nm) film. Pt was selected as a seed layer to enhance the PMA by promoting face-centered-cubic (111)-textured growth of the Co/Ni films[64], [65]. Although certain layers have attributed thicknesses below a single lattice spacing, it is understood that this refers to a fractional monolayer coverage by that particular layer. The nominal layer thickness of Co and Ni were obtained using a 6 MHz quartz crystal thickness monitor (Inficon, Inc., Switzerland). A Co(0.2 nm) layer was added for symmetry and capped with 3 nm thick Pt layer to prevent metal oxidation. The films were patterned into microdisks of 7 µm diameter by a lift-off technique using nLof2020 photoresist (MicroChemicals GmbH, Wiesbaden, Germany). Following the same procedure, microdisks with identical 7 µm diameter were patterned on the 500 µm thick single crystalline Si (001) substrate without the electrodes to assess possible effects of the substrate roughness.

3.3 Characterization methods

Various characterization methods were used to characterize the samples. In this section, we introduce the measured physical quantities and describe how measurements were made.

a. Surface Roughness

A BRUKER ICON (Bruker, Goleta, CA) atomic force microscope (AFM) was used to measure the surface roughness of the Pt film on the PMN-30PT and Si substrates by scanning regions of lateral extent 20 µm x 20 µm and 10 µm x 10 µm respectively at 1 Hz in tapping mode. A CoCrcoated AFM tip with a resonance frequency of 75 kHz was used for imaging. The average arithmetic roughness (R_a) was calculated from 2.5 µm x 2.5 µm area at five different locations on the flattened image.

b. Shape variations in Co/Ni microdisks

A FEI Nova 230 scanning electron microscope was used to visualize the shape variation in Co/Ni microdisks. Images were collected using an acceleration voltage of 3 kV following a working distance of 5.7 mm. The ImageJ[66] software was used to determine the perimeter and area of 63 microdisks. The microdisk's circularity (C) was calculated by the following Eq. (3.1),

$$C = \frac{4\pi * Area}{(Perimeter)^2} \tag{3.1}$$

c. In-plane strain

Two axial strain gauges with a gauge factor of 1.51 and gauge resistance of 120 Ω (Omega Engineering Inc.) were used to measure electric field-induced strain in the PMN-PT substrate. The change in the strain gauge resistance was monitored using an amplified signal from a Wheatstone bridge and recorded by an analog to digital converter (NI DAQ with NI-9237 module in a quarter bridge configuration). The strain gauges were bonded to the PMN-30PT substrates with top and bottom electrodes and excited with a voltage of 375 V to generate an electric field of 0.75 MV/m.

d. Magnetization and magnetic anisotropy

A superconducting quantum interference device (SQUID) magnetometer was used to determine the in-plane and out-of-plane magnetization of the films on PMN-PT. SQUID magnetometry was performed using a Quantum Design MPMS©3 SQUID magnetometer at 298 K. The in-plane and out-of-plane magnetizations were determined by sweeping the magnetic field from -1 T to 1 T.

e. Magnetic coercive field

A magneto-optic Kerr effect (MOKE) system was used to visualize the magnetization reversal process in the Co/Ni microdisk arrays on both the PMN-30PT and Si substrates. The magnetic field was applied perpendicular to the heterostructures while monitoring the real-time magnetization reversal process. Magnetic domain imaging was carried out using a Leitz Orthoplan polarizing microscope in reflection mode, monitored by a 4 Megapixel CCD camera (Thorlabs 4070M-USB). One full cycle of the recorded video was 100 seconds. The frame rate for video recording was 12 frames per second with sweeping rate 1.85 mT/sec for the PMN-30PT samples. Three frames were taken per second for the Si samples with sweeping rate 1.99 mT/s. The range of the applied magnetic field was -46.20 mT to 46.20 mT with an interval 0.16 mT for the microdisks on the PMN-30PT substrate, and from -49.79 mT to 49.79 mT with the interval of 0.67 mT for the microdisks on the Si substrate, respectively. The measurement was performed with five values of electric field, {0, 0.2, 0.4, 0.6, 0.8} MV/m, applied to the substrate.

Figure 3.2(a) and Figure 3.2(b) show the MOKE images of the magnetization reversal under a time varying magnetic field used to obtain the coercive field value of the individual microdisks. The $\mu_0 H_C$ of the individual Co/Ni microdisks were obtained from images extracted from the video with the applied magnetic field at different magnitudes. A curve of the contrast intensity (i.e. Kerr intensity) as a function of the applied magnetic field was generated for each microdisk. The magnetization reversal was often accompanied by more than one discrete remagnetization jump, indicating significant domain wall pinning during reversal. When the hysteresis loop of a microdisk displayed more than one magnetization jump during reversal, the final jump in the magnetization within a transition (e.g. from up-to-down) was attributed to the coercive field ($\mu_0 H_C$) value for the microdisk as depicted in Figure 3.3(a) and Figure 3.3(b). The slope observed in the hysteresis loop is due to the Faraday effect and does not affect the coercive field measurement. The median of $\mu_0 H_C$ was calculated from the measured $\mu_0 H_C$ values of the microdisks on the PMN-30PT and the Si substrates.

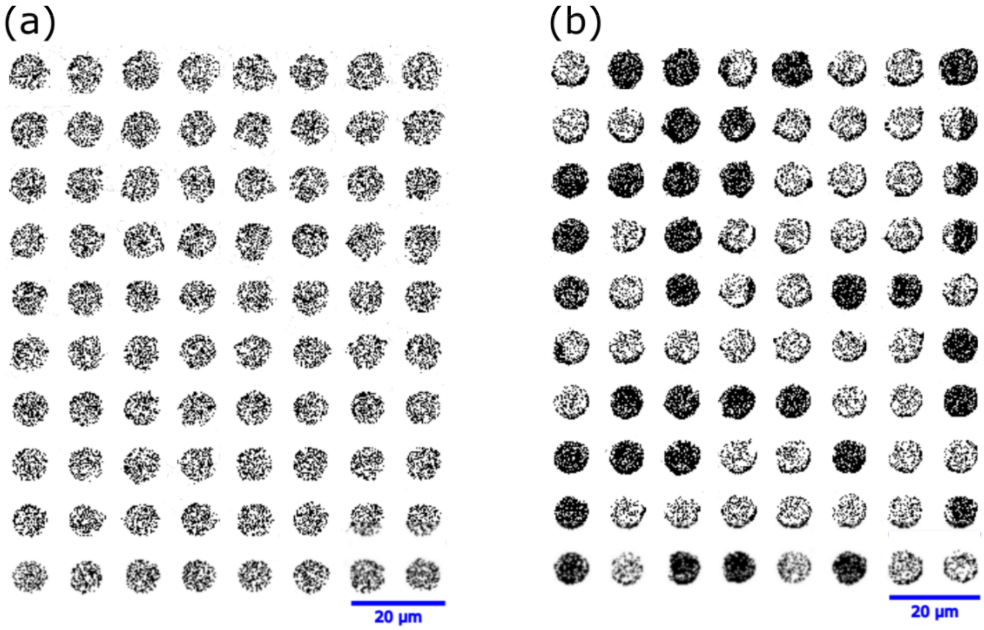

Figure 3.2. MOKE imaging of the microdisks on the PMN-30PT substrate under the magnetic fields (a) 0 mT (b) 37.8 mT. The light and dark contrast corresponds to the magnetization pointing up and down with respect to the substrate surface.

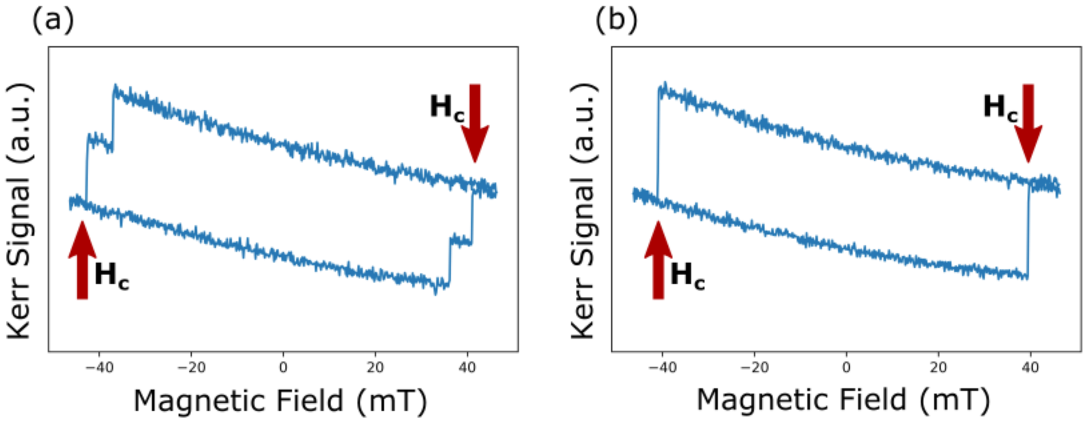

Figure 3.3. Illustration of a MOKE hysteresis loop with (a) multiple jumps (b) single jump.

3.4 Results and discussions

a. Contributors to non-uniform magnetization switching behaviors on PMN-30PT

A contour map was created to visualize the average coercive field of each disk to understand the variation in the coercive field among the microdisks. The results are shown in Figure 3.4(a) and Figure 3.4(b) for the eighty microdisks on the PMN-30PT substrates, respectively. The data on PMN-30PT were acquired in the absence of an electric field. Lateral inhomogeneity in the coercivity of Co/Ni microdisks is observed in both cases. The $\mu_0 H_C$ median for the Co/Ni microdisks on the PMN-30PT substrate was found to be 37.31 mT, whereas the $\mu_0 H_C$ median for the Co/Ni on the Si substrate was 29.95 mT, more than twenty percent lower in magnitude.

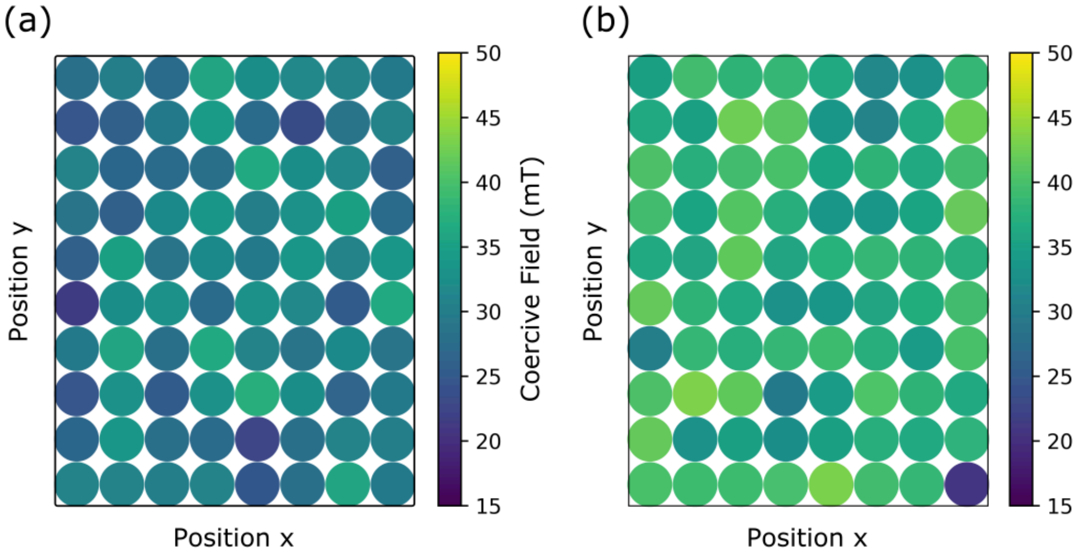

Figure 3.4. The coercive field distribution of an 8 by 10 array of microdisks on (a) Si and (b) PMN-30PT substrates. Each circle represents a microdisk.

In prior work, the laterally non-uniform behavior of the magnetization reorientation of heterostructures on a PMN-30PT substrate was attributed entirely to local strain variations arising from the domain structure in the PMN-30PT substrate[54]. However, here we have additionally demonstrated $\mu_0 H_C$ variations across the arrays of the Co/Ni microdisks on both PMN-30PT and Si substrates, where the Si substrate does not possess local variations in strain and has significantly lower surface roughness. This indicates that there are additional contributions to the variations in the coercive field across the microdisk arrays. Surface roughness of the substrate and lateral inhomogeneity of the Co/Ni microdisks appear to be the most significant contributors to the non-uniform $\mu_0 H_C$ distribution.

Recent studies have shown that the coercivity of deposited films is affected by the surface roughness of the substrate [57], [58], [67]. The average R_a of Co/Ni microdisks on PMN-30PT substrate was (2.8 ± 0.4) nm and that of Pt film on PMN-30PT was (2.2 ± 0.3) nm. Both are significantly larger than that of Co/Ni film on Si, which was measured as (0.6 ± 0.1) nm. Uncertainties reflect the one sigma variance of the estimated arithmetic roughness. The higher roughness of the PMN-30PT surface produces a higher local depinning field[58], defined as the external magnetic field required to move domain walls from pinning sites. The nearly 25% increase in coercivity for Co/Ni microdisks on PMN-30PT likely implies a larger depinning field for domain walls than for microdisks grown directly on a Si substrate.

Lateral inhomogeneity in the coercivity of Co/Ni microdisks and roughness due to substrate choice were addressed in the previous paragraph. In order to understand the inhomogeneity caused by micromanufacturing, the dimensions of the 63 Co/Ni microdisks were measured by SEM. The average circularity of the microdisks was (0.18 ± 0.05), which is particularly low and is a strong deviation from the nominal circular disk shape that was intended for the patterned disks. Uncertainty reflects the one sigma variance of the estimated circularity across over 63 microdisks. The nearly 30 % uncertainty of average circularity implies that variations and imperfections in the microfabrication process aids to the non-uniform $\mu_0 H_C$ distribution observed in the Co/Ni microdisks.

b. Strain effect on the coercivity of the Co/Ni microdisks

Now that the underlying factors contributing to the non-uniform variation in the coercive field of the microdisks on PMN-30PT have been articulated, the magnetoelectric performance of the microdisks is examined. Figure 3.5(a) and Figure 3.5(b) show the change of $\mu_0 H_C$ correlated to the initial $\mu_0 H_C$ at zero applied electric field for the entire family of 80 microdisks under electric fields of 0.2 MV/m and 0.8 MV/m respectively. The corresponding strain values of the applied field to the PMN-30PT substrate can be found in Figure 3.6. The red data points represent microdisks that exhibited multiple jumps during the magnetization reversal process as seen in Figure 3.3(a). Figure 3.5(c) and Figure 3.5(d) shows the microdisks with single-jump magnetization reversal processes denoted by blue dots to distinguish the coercive field distribution under the application of increasing electric fields. After removing the red data points, it remains evident that the coercive field distribution across the microdisks is shifted towards lower $\mu_0 H_C$ values as the magnitude of the applied electric field was increased from 0.2 MV/m to 0.8 MV/m, signifying the magnetoelectric effect on microdisk reversal.

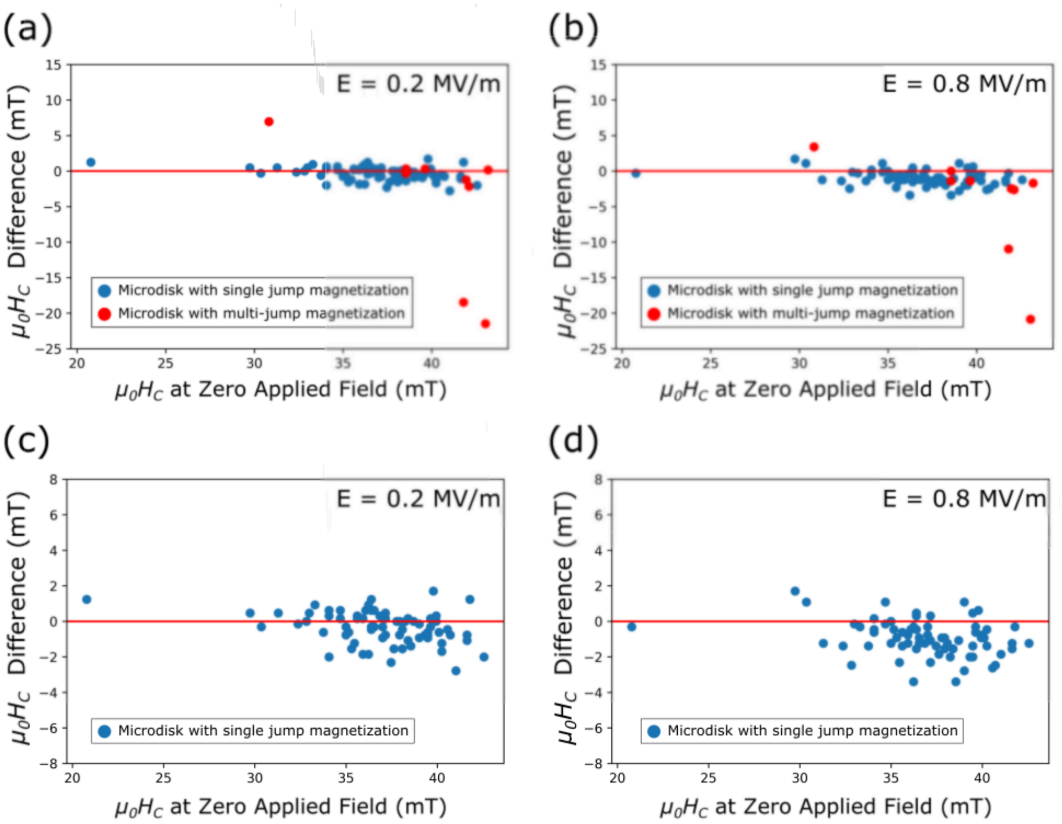

Figure 3.5. Scatter plots of µ0HC at zero applied E-field versus the µ0HC difference under the applied electric fields (a) between 0 MV/m and 0.2 MV/m (b) between 0 MV/m and 0.8 MV/m. (c) and (d) represent the microdisks with a single µ0HC value in (a) and (b), respectively.

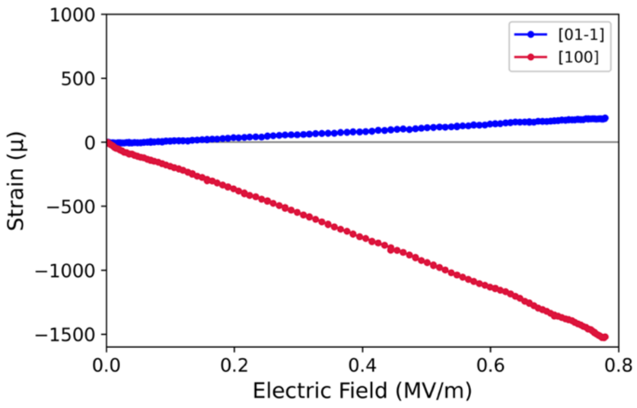

Figure 3.6 The in-plane strain components produced in the PMN-30PT as a function of out-of-plane electric field in both [01-1] and [100] directions

Figure 3.7 shows the calculated $\mu_0 H_C$ median for the microdisks with single jump magnetization reversal versus the external applied electric field on the PMN-30PT substrate. The trend in Figure 3.7 reflects the magnetoelectric coupling between the PMN-30PT substrate and the magnetostrictive Co/Ni microdisks. As the electric field-induced strain increases, the average coercive field of the Co/Ni microdisk array decreases due to the change in magnetoelastic energy. This corresponds to a reduction in the energy barrier for magnetization reversal, and a reduction in the perpendicular anisotropy energy. The weakened PMA is consistent with the strain-induced change in the magnetoelastic energy, and interfacial anisotropy modulation via strain has been observed in other Co-based multilayers[68]. However, the largest change in $\mu_0 H_C$ under an electric field is less than the difference between the coercive fields of the magnetic structures on the Si substrate and the PMN-30PT substrate at zero applied electric field. The $\mu_0 H_C$ median of Co/Ni microdisks on the Si substrate shows smaller coercivity than that of Co/Ni microdisks on the PMN-30PT substrate under each applied electric field. This implies the surface roughness effect is larger than the magnetoelastic effect on the coercivity of the patterned microdisks.

The standard deviations (SDs) of $\mu_0 H_C$ at a zero field were used as a comparison of the coercive field dispersion across the arrays on both PMN-30PT and Si substrates. The $\mu_0 H_C$ standard deviations of the microdisks on PMN-30PT substrate were [3.34, 3.15, 3.31, 3.29, 3.19] mT for the applied field [0, 0.2, 0.4, 0.6, 0.8] MV/m respectively, and that on Si substrate was found to be 3.46 mT. The coercivity standard deviation values of 3.34 mT and 3.46 mT were found for Co/Ni microdisks on the PMN-30PT under zero applied field and Si respectively. The difference among the standard deviations for each of the applied fields were less than 0.2 mT. The values of $\mu_0 H_C$ dispersions do not show strong correlation with either the substrate roughness or the strain. The difference of the $\mu_0 H_C$ dispersions are more likely a consequence of edge roughness/circularity variation. The results indicate that surface roughness and strain shift the coercivity but do not affect the $\mu_0 H_C$ dispersions significantly.

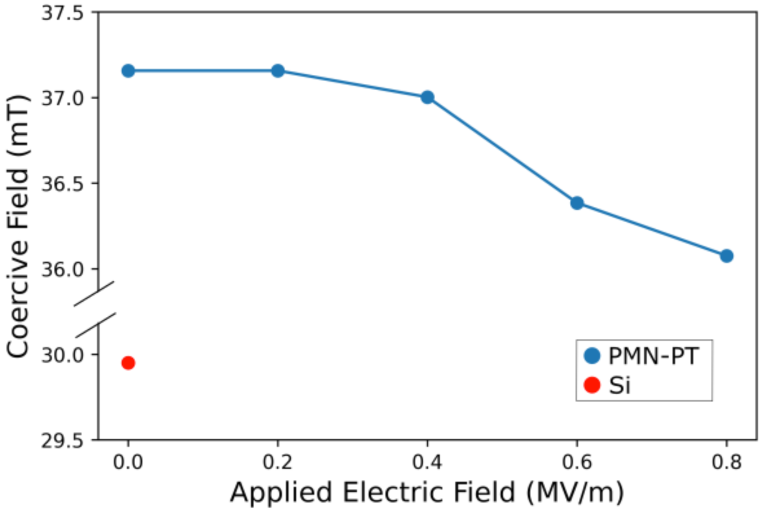

Figure 3.7. Median coercive field as a function of the applied electric field to the PMN-30PT and Si substrates.

c. Magnetoelastic energy discussion

In this section, magnitude of magnetoelastic energy density is compared with anisotropy energy density to understand the strain-induced coercivity. SQUID measurements were performed to obtain anisotropy field ($\mu_0 H_k$) and saturation magnetization (M_s). Figure 3.8 shows the hysteresis loop of Co/Ni films of both in-plane (IP) and out-of-plane (OOP) directions from the SQUID measurements. The results indicate easy axis out-of-plane. The $\mu_0 H_k$ was measured to be 0.4 T and the M_s was found to be 910 kA/m.

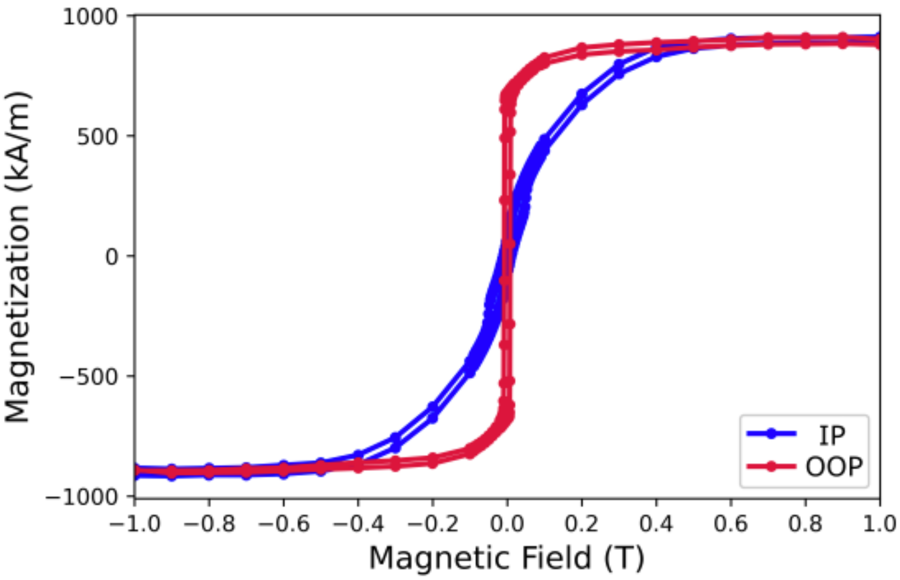

Figure 3.8. Hysteresis loop of Co/Ni films for both in-plane (IP) and out-of-plane (OOP) directions.

PMA Co/Ni films exhibit uniaxial anisotropy. The effective anisotropy energy density for the Co/Ni films can be expressed by Eq. (3.2)

$$E_{anistropy} = \frac{1}{2}\mu_0 M_S H_K \sin^2\theta \tag{3.2}$$

where μ_0 is permeability of free space; θ is the polar angle relative to the orientation normal to the sample. M_s and $\mu_0 H_k$ were estimated as 910 kA/m and 0.4 T from Figure 3.8.

The magnetoelastic energy density change was determined using the following equations[68]:

$$\Delta E_{me} = \frac{B_1}{6}\left(\varepsilon_x - \varepsilon_y\right) + \frac{B_2}{6}[5\varepsilon_x + \varepsilon_y + \frac{6\nu}{1-\nu} \times (\varepsilon_x + \varepsilon_y)] - \frac{B_1 + 2B_2}{3}\,(\varepsilon_x - \varepsilon_y) \tag{3.3}$$

where ε_x and ε_y are in-plane strains in [100] and [01-1] directions. ε_x =-1500 μ and ε_y= 500 μ under the field 0.8 MV/m can be found in supplementary information. Poisson's ratio ν = 0.3. B_1 and B_2 are expressed as a function of magnetostriction (λ_{100}, λ_{111}) and elastic constants (c_{11}, c_{12}, c_{14}) by Eq. (3.4) and Eq. (3.5)

$$B_1 = -\frac{3}{2}\lambda_{100}(c_{11} - c_{12}) \tag{3.4}$$

$$B_2 = -3c_{44}\lambda_{111} \tag{3.5}$$

Elastic constants of Ni were chosen for the approximation of B_1 and B_2 (c_{11} = 250 GPa, c_{12} = 160 GPa, c_{44} = 118.5 GPa), given that Ni and Co have comparable values of their elastic constant, respectively. Magnetostriction in Co/X multilayers[69], where X=Pt, Cu, Ag, Au has been observed with the order of magnitude 10^{-4}. This value was used for the estimated value of λ_{100} and λ_{111}. $E_{anistropy}$ was estimated to be on the order of 100 kJ/m^3, which is significantly larger than the contribution of magnetoelastic energy density (less than 10 kJ/m^3) induced by the applied electric field. This limited the total effect of magnetoelectric modulation on the Co/Ni microdisks, particularly with respect to engineering any significant rotation of the Co/Ni magnetization away from its out-of-plane easy axis. This is also consistent with the modest strain-induced 2.9% reduction of coercive field at 0.8 MV/m electric field in the PMN-30PT substrate.

3.5 Summary

In this chapter, Co/Ni microdisks were fabricated on PMN-30PT (011) and Si substrates and the effect of surface roughness, in-plane strain, and manufacturing defects were assessed. $\mu_0 H_C$ variations across the Co/Ni microdisk arrays were observed on both the Si and PMN-30PT substrates with zero applied field, and the standard deviations of the $\mu_0 H_C$ distribution were comparable for both arrays showing that surface roughness was not primary cause of the observed dispersion in $\mu_0 H_C$. This suggests that the $\mu_0 H_C$ variation was more likely the result of variations introduced in the fabrication process. The $\mu_0 H_C$ of Co/Ni microdisks on the PMN-30PT substrate was larger than that on the Si substrate by nearly 25%. The larger $\mu_0 H_C$ observed for the Co/Ni microdisks on the PMN-30PT specimen was attributed to an increase in the depinning field. Coercivity was measured with different applied electric field to the PMN-30PT. The results indicate that strain induced by the electric field lowers the $\mu_0 H_C$ of Co/Ni. The strain induced modulation of the coercivity is modest when compared to the contributions from surface roughness and patterning-induced disorder. The estimated anisotropy energy density was larger than the strain-induced energy density change with an order of magnitude difference. This also explains the limited strain effect on the modulation of coercivity. Design of strain modulated PMA based devices will require selection of material systems and processing technique that lead to lower interfacial roughness, and improved edge/sidewall uniformity of microstructures, in order to realize a smaller coercivity for strain induced coercive field modulation.

Chapter 4. Magneto-mechanical Effects in Atomic Spin Model

4.1 Introduction

Manipulation of magnetic spins at the atomic level has become an important research topic due to its wide range of potential applications such as the quantum simulator [70], quantum neuromorphic computing [71], and atomic spin-wave memory [72]. Atomically-driven ultrafast control of magnetization may lead to fast and energy-efficient data processing in the future [73]. As such, the recent interest in versatile atomic spin-based applications has driven the need for magnetic modeling techniques. Spin dynamics simulations were initially implemented based on density functional theory (DFT) in 1995 [7]. The theory of magnetic Hamiltonian was then widely studied in the early 2000s [9]. Combining DFT calculations and classical simulations helped reduce computational costs. Parameters extracted from DFT simulation and experiments were used in the simplified Hamiltonian to speed up calculations [5], [8]. Based on this multiscale framework, several codes have been developed such as ASD[10], SPIRIT[11], and VAMPIRE[12]. However, in existing atomic spin codes, exchange striction and magnetoelastic effects have not been taken into account. These effects are important to the control of magnetization states and dynamics of the atomic spin systems.

Exchange striction and magnetoelastic effects have been demonstrated to control magnetization to facilitate development of next generation magnetic devices [74]–[76]. Magnetization switching induced by magnetostrictive effects has been demonstrated in nanoscale magnetic heterostructures promising low energy consumption spintronics [77]. Such effects can also be used to control magnetizations at atomic scales. In addition, ferromagnetic resonance shows a strong dependence on the magnetostriction [78]. Magnetic resonance-based quantum computers show promise for reliable quantum computing [79]. The frequency modes of the system modified via exchange striction and magnetoelastic effects can be a promising way to control quantum bits[80], [81].

In this work, we study a system of two Co adatoms residing on a Cu(100) substrate. Such a system has been widely researched using a variety of experimental approaches looking at the Kondo effect and Ruderman–Kittel–Kasuya–Yosida (RKKY) interactions between Co adatoms [82]–[85]. These works have successfully demonstrated lateral atom manipulation and single spin orientation control in the Co/Cu system using the scanning tunneling microscope (STM) [86], [87].

Here, a phenomenological model of two Cu adatoms on a Cu substrate was developed using a multiscale approach. The atomic spin model uses parameters obtained from DFT calculations. Mechanical and magnetic degrees of freedom are coupled in the atomic spin model. Coupled Landau-Lifshitz (LL) equation[88], governing the magnetization dynamics, and Newton's equation of motion to govern the mechanical behavior are studied to demonstrate the mutual influence of magnetic and mechanical degrees of freedom. The exchange striction and magnetoelastic effects are introduced as correction terms to both the exchange and anisotropy constants. Correction terms are linearly dependent on the displacement between two adatoms. Hence, exchange striction and magnetoelastic effects are referred to as the "magneto-displacement" effect. The results demonstrate spin-flip and in-plane to out-of-plane transitions can be induced with the change of distance between two adatoms. Resonant frequencies of the system are studied and the manipulation of resonant frequencies is demonstrated.

4.2 Model

Multiscale modeling is performed from the quantum scale to the atomistic scale. Material properties such as anisotropy and exchange constants are first obtained from DFT calculations at the quantum scale. The constants are then introduced to the atomic scale phenomenological model. Force is exerted on the Co adatoms to change the atomic distance between them, and a magnetic field is used to control their magnetization orientation. The ground states of two atomic spins are obtained by minimizing the total energy of the system. The multiscale modeling enables the investigation of both the equilibrium and the dynamic magnetization states under different conditions.

a. Geometry

We consider a system consisting of two Co adatoms placed on a Cu(100) substrate as illustrated in Figure 4.1(a). Two Co atoms are placed on top of the substrate. The distance between the adatoms is *d*. Each Co atom possesses a magnetic moment. External magnetic field (B field) is applied to the system along the z-direction to study in-plane (IP) to out-of-plane (OOP) magnetic moment switching. Interaction of the adatoms with the substrate produces out-of-plane magnetic anisotropy. The distance between the adatoms is small. Therefore, the exchange interaction may exist between the adatoms. This interaction may appear through the conduction of electrons in the substrate. System symmetry (existence of the vector connecting the adatoms) implies that there could be in-plane uniaxial anisotropy contribution to the energy appearing due to spin-orbit interaction and substrate conduction electrons.

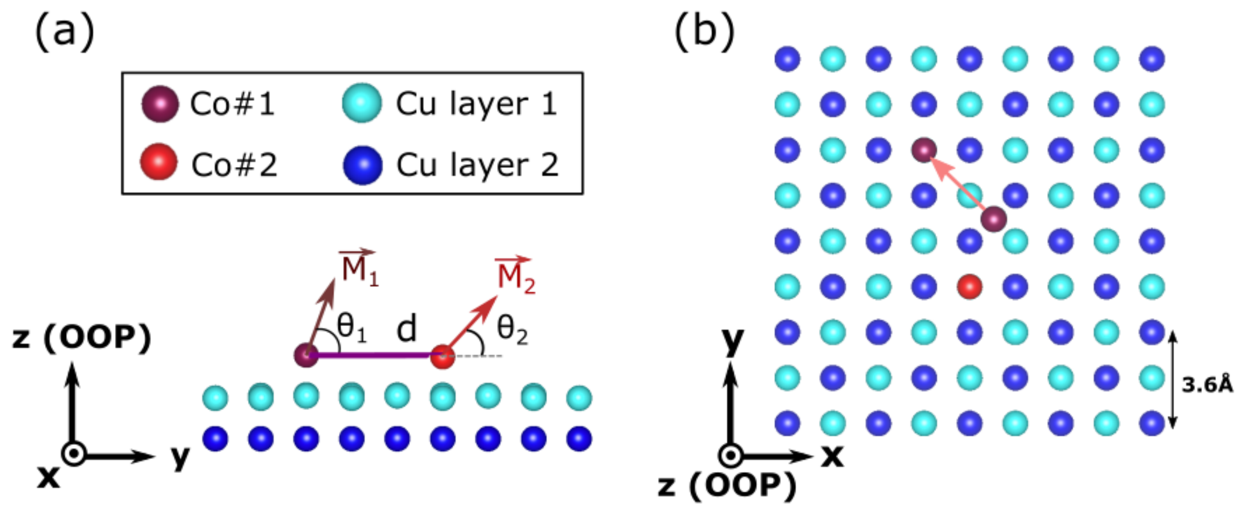

Figure 4.1. Schematic illustration of the proposed model. (a) side view of the two Co atomic spins on the Cu substrate. (b) top view of Co adatoms on the Cu substrate with an arrow indicating the moving path of Co#1.

b. Phenomenological model

To describe the behavior of two Co adatoms system phenomenologically, we Hamiltonian including spring energy, exchange interaction, and IP and OOP anisotropies. Magneto-displacement effects were incorporated in the phenomenological model through the dependence of the exchange and IP and OOP anisotropies on the distance between two Co adatoms. The distance between two Co atomic spins is expressed as

$$d = d_0(1 + \varepsilon) \tag{4.1}$$

where d_0 is the initial (equilibrium in the absence of forces) distance between two Co adatoms, ε is the normalized atomic displacement. The energy dependence on ε was linearized, assuming the change of distance is small.

In this work, the dipole-dipole interaction is not considered. Thermal effects were not taken into account in the model. Co adatom has an atomic moment of 2 μ_b (Bohr magneton). The orientations of atomic moments are defined by the angles θ_1 and θ_2 with respect to the y' axis, which is the axis connecting the two adatoms. $\vec{M}_1$ and $\vec{M}_2$ are normalized and expressed as

$$\vec{M}_1 = (0, \cos\theta_1, \sin\theta_1);\ \vec{M}_2 = (0, \cos\theta_2, \sin\theta_2); \tag{4.2}$$

The total energy is the sum of exchange energy E_{ex}, anisotropy energy E_{ani}, spring energy E_{sp}, and external field energy E_{ext}

$$E_{total} = E_{ex} + E_{ani} + E_{sp} + E_{ext} \tag{4.3}$$

The exchange energy E_{ex} depends on relative atomic spin orientation and the displacement of the adatoms,

$$E_{ex} = -(J_0 + J_1\varepsilon)\left(\vec{M}_1 \cdot \vec{M}_2\right) \tag{4.4}$$

where J_0 is exchange constant and J_1 is exchange striction constant. The anisotropy energy E_{ani} includes in-plane (y'-axis) and out-of-plane (z-axis) contributions.

$$E_{ani} = -\frac{1}{2}(K_0^z + K_1^z\varepsilon)({\vec{M}_{1z}}^2 + {\vec{M}_{2z}}^2) - \frac{1}{2}\left(K_0^{y'} + K_1^{y'}\varepsilon\right)({\vec{M}_{1y'}}^2 + {\vec{M}_{2y'}}^2) \tag{4.5}$$

where $K_0^{y'}$ and K_0^z are anisotropy constants, $K_1^{y'}$ and K_1^z are magnetoelasticity constants in both y' and z directions, respectively. The Co adatoms have strong exchange coupling due to small distance between them. Therefore, same anisotropy constants are used for both adatoms.

The spring energy E_{sp} is given by

$$E_{sp} = \frac{1}{2}k\,(d_0\,\varepsilon)^2 - f_0 d_0 \varepsilon \tag{4.6}$$

where k is the spring constant of the system, and f_0 is the external force applied to the system. Finally, the interaction with external field $\vec{H}$ is determined by the expression

$$E_{ext} = -\vec{H} \cdot 2\mu_b\left(\vec{M}_1 + \vec{M}_2\right). \tag{4.7}$$

Minimizing the energy over magnetization orientations and the distance between the adatoms one defines the system equilibrium state. Beside the equilibrium state, the eigenfrequencies of the system can be found by solving coupled Landau-Lifshitz and Newton's equations.

$$\frac{\partial \vec{M}_1}{\partial t} = \gamma \vec{M}_1 \times \vec{H}^1_{eff}, \tag{4.8}$$

$$\frac{\partial \vec{M}_2}{\partial t} = \gamma \vec{M}_2 \times \vec{H}^2_{eff}, \tag{4.9}$$

$$-\frac{\partial E_{total}}{\partial d} = m_{co} \ddot{d}\,. \tag{4.10}$$

where γ is the gyromagnetic ratio and m_{co} is the mass of Co atom. The effective fields for $\overrightarrow{M_1}$ and $\overrightarrow{M_2}$ are given by

$$\vec{H}^1_{eff} = -\frac{\partial E_{total}}{\partial \overrightarrow{M_1}} = (J_0 + J_1\varepsilon)\vec{M}_2 + (K_0^z + K_1^z\varepsilon)\vec{M}_{1z} + \left(K_0^{y'} + K_1^{y'}\varepsilon\right)\vec{M}_{1y'} + \vec{H}, \tag{4.11}$$

$$\vec{H}^2_{eff} = -\frac{\partial E_{total}}{\partial \overrightarrow{M_2}} = (J_0 + J_1\varepsilon)\vec{M}_1 + (K_0^z + K_1^z\varepsilon)\vec{M}_{2z} + \left(K_0^{y'} + K_1^{y'}\varepsilon\right)\vec{M}_{2y'} + \vec{H}\,. \tag{4.12}$$

The force acting on the second adatom is given by

$$-\frac{\partial E_{total}}{\partial \varepsilon} = \tag{4.13}$$

$$J_1\, \vec{M}_1 \cdot \vec{M}_2 + \frac{K_1^z}{2}\left(\vec{M}_{1z}^{\ 2} + \vec{M}_{2z}^{\ 2}\right) + \frac{K_1^y}{2}(\vec{M}_{1y'}^{\ 2} + \vec{M}_{2y'}^{\ 2}) - k d_0^2 \varepsilon + f_0 d_0$$

Only linearized equations are considered here. The perturbation of the magnetic moments and interatomic distance are given by $\overrightarrow{m_1}$, $\overrightarrow{m_2}$, and ε_p giving

$$\vec{M}_1 = \vec{M}_{s1} + \vec{m}_1 e^{i\omega t}, \tag{4.14}$$

$$\vec{M}_2 = \vec{M}_{s2} + \vec{m}_2 e^{i\omega t}, \tag{4.15}$$

$$\varepsilon = \varepsilon_0 + \varepsilon_p e^{i\omega t}, \tag{4.16}$$

where ω is eigenfrequency; $\vec{M}_{s1}$ and $\vec{M}_{s2}$ are the equilibrium magnetic moments of Co#1 and Co#2 atoms; ε_0 is the equilibrium atomic displacement.

c. Density functional theory (DFT) simulations

The parameters J_0, $J_1, K_1^z, K_2^z, K_1^{y'}, K_2^{y'}$ in Eqs. (4.4) and (4.5) are defined using the DFT simulations. The simulated system is shown in Fig. 1(a) and (b). In our DFT model, the substrate is a two-layer 9-by-9 grid of Cu atoms with a lattice constant of 3.6 Å. The adatom Co#1 is fixed in the simulations on top of the underlying Cu atom. The second adatom is moved along the line show by the red arrow in Figure 4.1(b). This allows to change the inter-adatom distance d and study the distance-dependent magnetic interactions. The lattice constant of the substrate did not change and no substrate strain effect was involved in the DFT calculation. The position of both Co adatoms was relaxed along z-direction (OOP). The simulations are performed at zero temperature.

Structural relaxation was carried out using the Vienna Ab initio Simulation Package (VASP) [89], [90] within the generalized gradient approximation as parameterized by Perdew et al. [91] until the largest atomic force was smaller than 0.01 eVÅ-1. The pseudopotential and wave functions were treated within the projector augmented-wave method [92], [93]. A 15-Å-thick vacuum region was introduced to separate the periodic slabs along the stacking direction. The plane wave cutoff energy was set to 500 eV.

For each position of Co#1, the total energy of the system was calculated for both ferromagnetic (FM) and anti-ferromagnetic (AFM) ordering of the two Co adatoms, where in each case various magnetization directions along [100], [010], [001], [110], and [1-10] were considered as an initial condition for the relativistic DFT calculations. The total energy consists of four terms, e.g., spring energy, exchange interaction, IP anisotropy, and OOP anisotropy energy. We then used a linear regression method to fit the results to a phenomenological model (described in the following section) and found the coefficients for the exchange energy and anisotropies energies as a function of the distance between two Co adatoms. The spring energy is independent of magnetic states. The anisotropic exchange energy is negligible; thus, we show the anisotropy energy generated from ferromagnetic ordering as the representative result for both IP and OOP anisotropy energy terms. We found that the Co magnetic moments are close to 2 μ_b (Bohr magneton).

4.3 Results

a. DFT results

In Figure 4.2, each energy is plotted against the distance between two Co adatoms. Figure 4.2(a) describes the spring energy variations with the distance between two Co adatoms, and indicates that the stable positions of two Co adatoms occurs when they are separated 3.6 Å and 5.7 Å apart. The elastic constant (k) is found to be 3.6 eV by a second-order curve fitting with a function $\frac{1}{2}kx^2$ at the distance 5.7 Å. Oscillation of the spring energy occurs obviously from periodicity of the substrate lattice. The equilibrium positions corresponds to the first adatom located on top of the place in between the Cu atoms (see Figure 4.3).

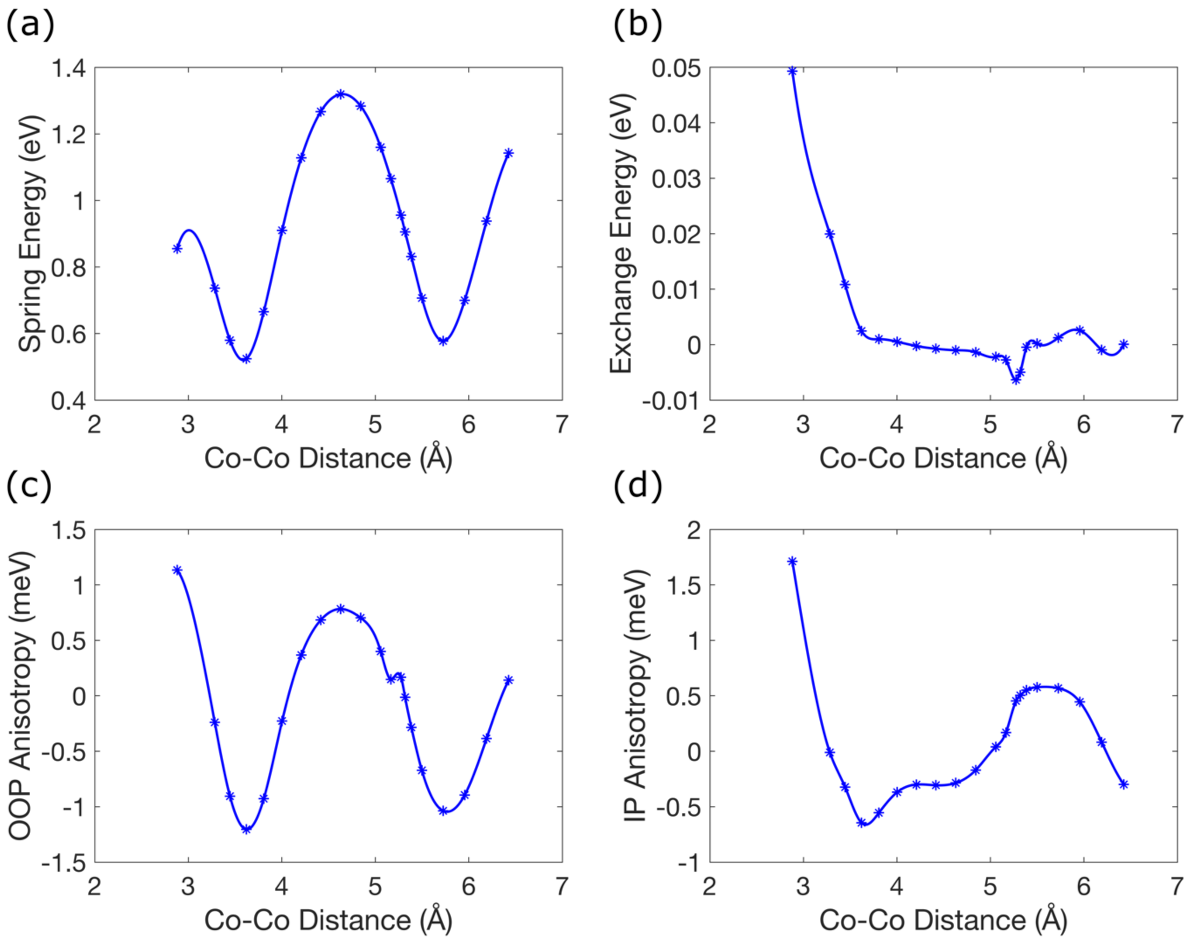

Figure 4.2. The different energy terms as a function of the distance between the two Co adatoms. (a) Spring energy (b) Exchange energy (c) OOP anisotropy (d) IP anisotropy.

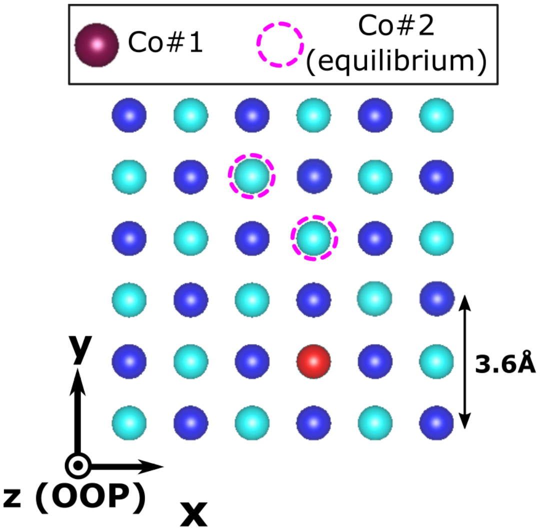

Figure 4.3. The dashed circles indicates two equilibrium positions of Co#2 at the distance of 3.6 and 5.7 Å between two adatoms.

In Figure 4.2(b), the exchange energy starts positive and decreases as the adatoms are moved further apart. Oscillations occur at larger atomic distances because the exchange interaction is mediated by the conduction electrons in the Cu substrate. This mechanism is similar to RKKY. Negative exchange energy gives an antiferromagnetic (AFM) stable state, and a positive value leads to a ferromagnetic (FM) coupling. At the distance 5.7 Å, the exchange energy oscillates between positive and negative values. We focus on this region to investigate the FM to AFM transition induced by the exchange striction effect. J_0 is 0.003 eV and J_1 was found to be -0.077 eV at Co-Co distance around 6Å, close to the equilibrium state.

The OOP and IP anisotropy energies versus the Co-Co distance are depicted in Figure 4.2(c) and (d), respectively. The OOP anisotropy oscillates between positive and negative numbers, whereas IP anisotropy reduces to near zero as the Co-Co distance increases. The oscillation of OOP anisotropy is attributed to the bonding between Cu substrate and Co adatoms. The two minimum energy points observed at 3.6 or 5.7 Å agrees with the spring energy results in Figure 4.2(a). IP uniaxial anisotropy is associated with the interaction between two Co adatoms. As the distance increases, the anisotropy reduces to zero. For the equilibrium state around 5.7Å, the values of anisotropy constants are $K_0^{y'} = 0.5\, meV,\ K_1^{y'} = -8.5\, meV,\ K_0^{z} = -1\, meV, K_1^{z} = 12\, meV.$

b. FM to AFM transition (spin flip)

The phenomenological model with the parameters obtained with DFT simulations was used to study equilibrium state and resonance frequencies of two adatoms as a function of displacement. There is no external magnetic field applied to the adatoms. A force term is introduced to the phenomenological Newton's equation Eq. (4.13) to change the distance between the adatoms. Figure 4.4 illustrates the transition from the FM to AFM state as the distance between the two Co adatoms is increased. In Figure 4.4(a), the magnetic state is initialized with the FM state at $\varepsilon = 0$. As Co#1 and Co#2 are separated farther, the positive exchange constant becomes negative. One of the atomic spins flips 180 degrees and transitions to an AFM state. In this region, the value of exchange constant spans positive to negative values.

The magnetoelastic effect can assist the FM to AFM transition. In Figure 4.4(b), the external force f_0 is varied while monitoring the change of ε. f_0 and ε are approximately linearly related, except an abrupt change between ε ~0.038 to 0.040. This abrupt change in Figure 4.4(b) occurs at the magnetization transition from FM to AFM in Figure 4.4(a), confirming that the magnetic state transition affects the effective spring constant of the system.

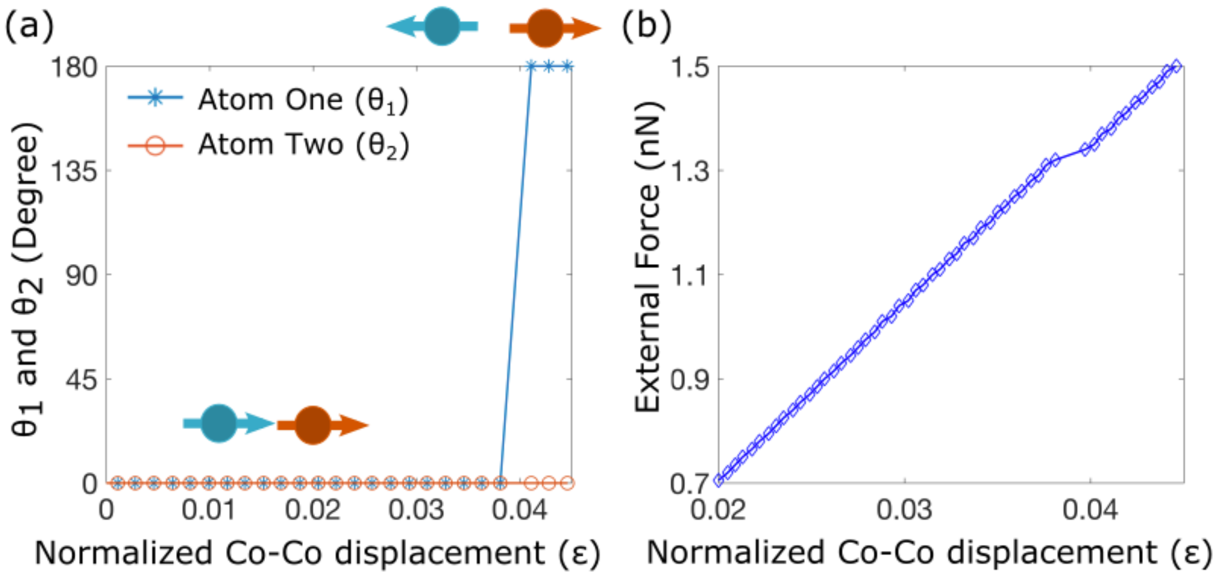

Figure 4.4. FM to AFM transition assisted with exchange striction effect. (a) Co atomic magnetization orientation as a function of normalized Co-Co displacement (b) Normalized Co-Co displacement response to an external force applied to the system.

The phenomenological model enables us to study the dynamic magnetic behavior of the system. The system has three degrees of freedom, which gives three resonance frequencies. Figure 4.5 shows the three eigenfrequencies of the system and their dependence on ε. While all degrees of freedom are coupled but not purely mechanical motion and purely magnetic oscillations, we are still able to distinguish predominantly magnetic and predominantly mechanical oscillations. Two “magnetic frequencies” are mostly related to exchange and anisotropy energies. The “mechanical” frequency is mostly related to spring energy. The exchange mode corresponds to out-of-phase magnetization precession of two magnetic moments. One can estimate it as $(J_0 + J_1\varepsilon)/(2\gamma\mu_b)$. The anisotropy mode corresponds to in-phase precession of magnetic moments. This frequency is defined by the anisotropy constants $(K_0^z + K_1^z\varepsilon)/(2\gamma\mu_b)$ and $\left(K_0^{y'} + K_1^{y'}\varepsilon\right)/(2\gamma\mu_b)$. Mechanical frequency describes the mode of vibrations and is determined by the spring constant.

As we change the distance between the adatoms, the magnitude of mechanical frequency is the largest and remains constant due to the weak influence of the magnetic degrees of freedom on the mechanical mode. Exchange frequency reaches a minimum where the FM to AFM transition happens and the exchange coupling constant becomes close to minimum $\frac{(J_0+J_1\varepsilon)}{2\gamma\mu_b}$. For the anisotropy frequency, the anisotropy effect reduces with the increase of atomic distance.

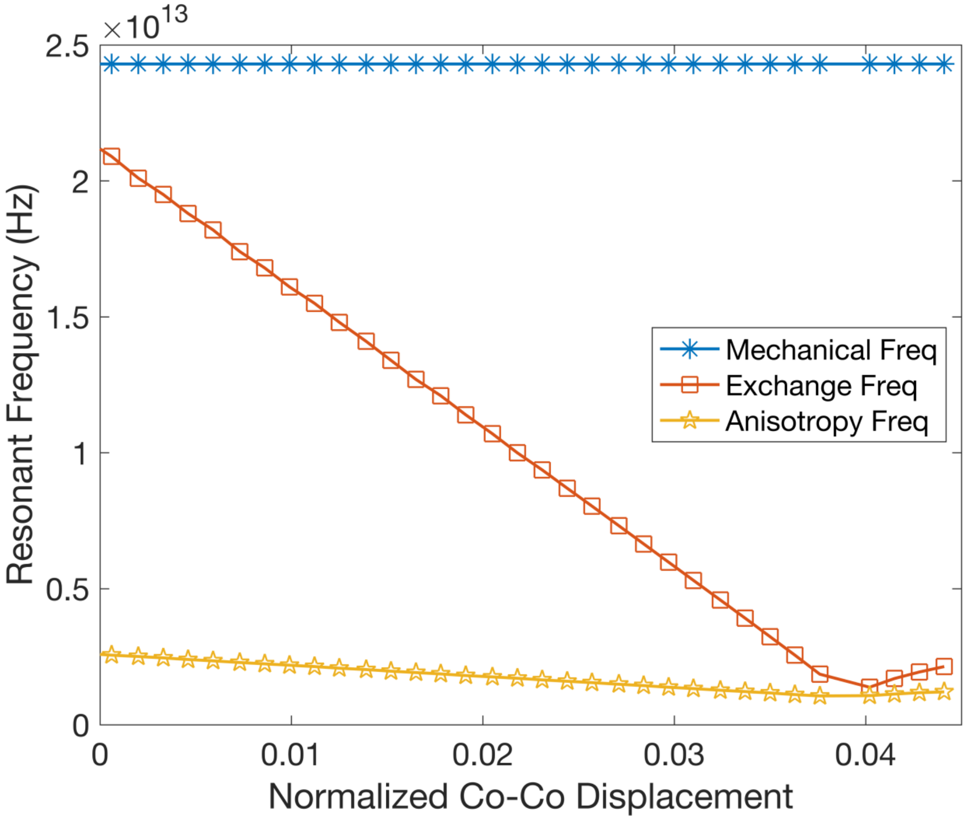

Figure 4.5. “Mechanical”, “exchange”, and “anisotropy” frequencies as a function of normalized Co-Co displacement. They are named based on their main contributions. Mechanical frequency is dominated by the mechanical interaction between two adatoms; exchange frequency is mainly contributed by the exchange interaction of two atomic spins; anisotropy frequency is largely attributed to magnetic anisotropy.

c. In-plane (IP) to out-of-plane (OOP) switching assisted by magneto-displacement effect

Here we consider the case where the out-of-plane magnetic field (z-direction) is applied to the in-plane magnetic state (along the y-axis) to investigate IP to OOP switching. The values of the parameters are the same as those used in the cases above. Two cases with different displacement are studied. At $\varepsilon = 0$, the values of anisotropy constants for OOP and IP orientation are $K^{z} = -1\, meV$ and $K^{y'} = 0.5\, meV$, respectively. At $\varepsilon = 0.056$, the corresponding anisotropy constants are $K^{z} = -0.3\, meV$ and $K^{y'} = 0.02\, meV$. Figure 4.6(a) shows the orientation of atomic magnetic moments as a function of the applied field at $\varepsilon = 0$. In this case the zero applied field state is the FM state. As the external field is applied Co magnetic moments stay in the FM state, but the orientation becomes canted with respect to the substrate plane. The IP to OOP state transition completes at the external field of 13 T. In the second case the normalized atomic displacement ($\varepsilon = 0.056$) is introduced. The equilibrium state in this case if the AFM one (Figure 4.6(b)). The field required for the IP-OOP transition in this case is about twice high as the one without the applied ε. This is because the external field has to overcome both magnetic anisotropy and the AFM exchange interaction to attain the transition to OOP state.

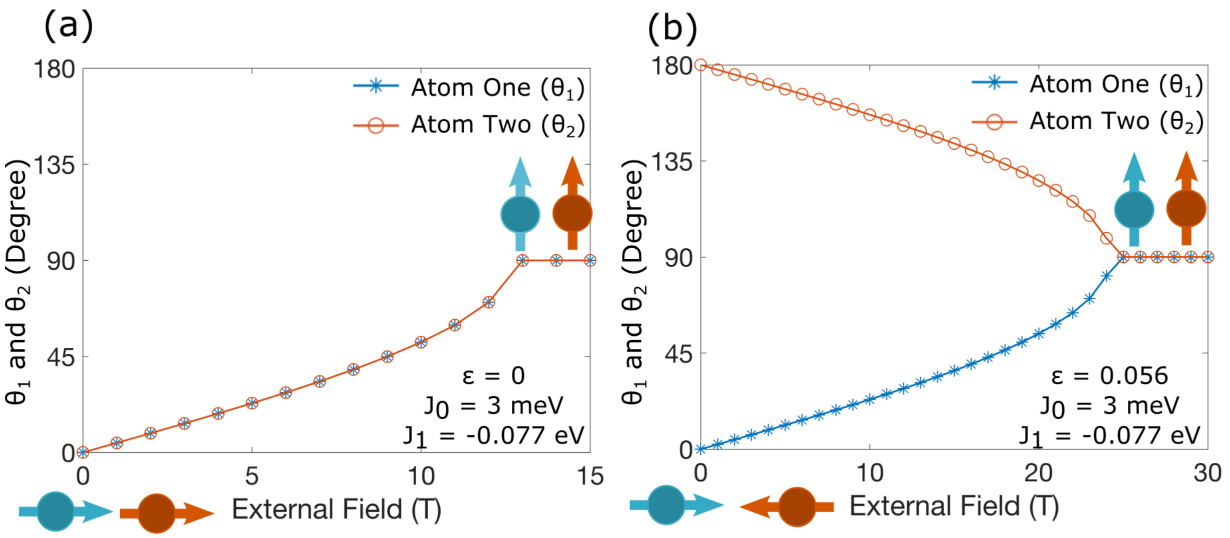

Figure 4.6. Magnetic moment orientations of two Co atoms as a function of external magnetic field in the z-direction with positive J_0, negative J_1, and (a) $\varepsilon = 0$ (b) $\varepsilon = 0.056$.

Next, we investigate the other hypothetical case where we reverse signs of the constants J_0 and J_1 and the anisotropy terms remains the same as the previous case. In this case the system is initialized with AFM ground state. Dependence of the magnetic state on the external field is shown in Figure 4.7. For zero relative displacement ($\varepsilon = 0$), IP to OOP switching occurs at an external applied field of 64T. After applying the atomic displacement ($\varepsilon = 0.056$), the required field significantly reduces to 3T (Figure 4.7 (b)). The reduction of the required field needed for the AFM to FM transition is much greater than that in the previous case with FM state. In both cases, we find that the required magnetic field for switching can be significantly changed due to magneto-displacement effects.

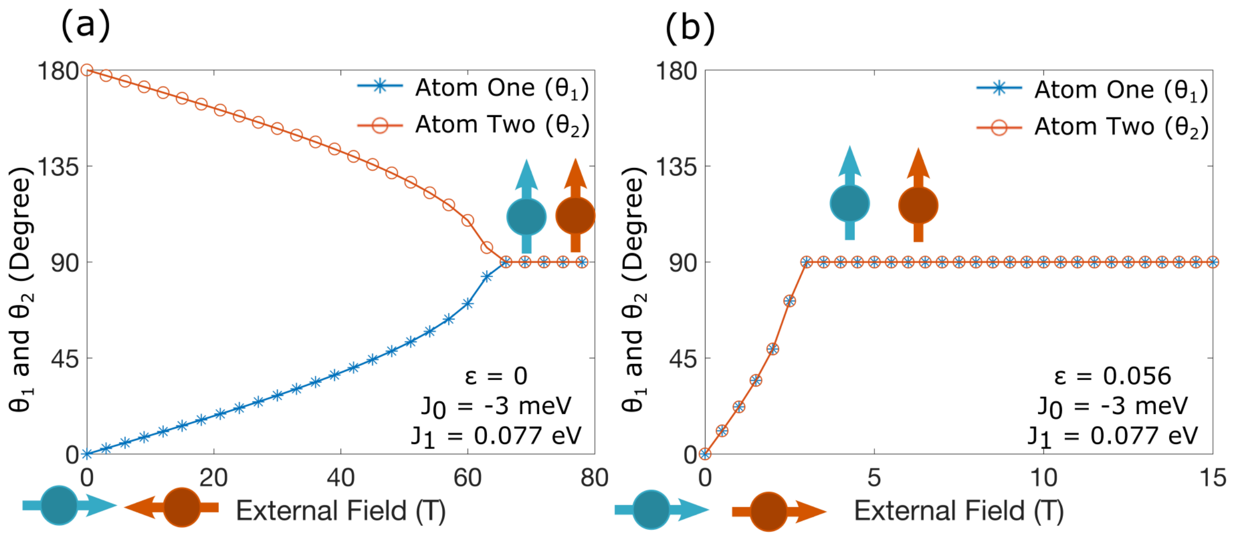

Figure 4.7. Magnetic moment orientations of two Co atoms as a function of external magnetic field in z direction with negative J_0, positive J_1, and (a) $\varepsilon = 0$ (b) $\varepsilon = 0.056$.

4.4 Discussion

The adatom manipulation discussed in the present work can be realized experimentally using the tip of scanning Tunneling Microscope (STM). It was first used to demonstrate lateral positioning of atoms on the surface by Eigler and Erhard [94]. The STM technique enables a Co adatom to move on the Cu substrate and manipulate the lateral atomic distance between two Co adatoms by tip-induced potential [86]. Spin-polarized STM (SP-STM) has been used to image atomic spin direction with a polarized tip [87]. SP-STM is a potential technique to monitor the magnetization transition of Co atomic spins. In addition to the static magnetization measurements, magnetic resonance of single atomic spin can be obtained by combining STM and electron spin resonance (ESR) [95]. This allows monitoring the resonant frequency change of the system. Another option to manipulate the distance between the adatoms is through the applied mechanical strain to the substrate. This can be done by integrating with a piezoelectric layer under the Cu substrate. This work does not incorporate an induced strain in the substrate. However, the same phenomenological model can be used to study the strain effects, providing a set of DFT parameters are generated under varying lattice constants of the substrate.

4.5 Conclusion

A model of two Co adatoms residing on a Cu(100) substrate was developed incorporating magneto-displacement effects as correction terms to the exchange and anisotropy constants in a phenomenological model. The parameters used in the spin model were extracted from DFT calculations. Coupled LL equation and Newton's law governed the dynamics of the system. We observed a FM to AFM transition as the distance between the two Co adatoms was increased. A wide range of resonance frequencies of the system can be tuned with the change of atomic distance. The required magnetic field to achieve IP to OOP transition is significantly reduced by changing the interatomic distance. The results provide an understanding of the displacement effect on the atomic magnetization behavior that can assist the advancement of atomic-scale devices.

Chapter 5. Conclusion and Outlook

This dissertation focused on the development of magnetoelectric microdevices and multiscale modeling. Specifically, multilayer Co/Ni was studied due to its large PMA and tunability of saturation magnetization. Patterned Co/Ni multilayers were proposed for a cell sorting application. Integrated Co/Ni devices were further studied to better understand the roughness and magnetoelectric effects on the uniformity of magnetic response. In the modeling work, the magnetization state and dynamics of the atomic spin systems were investigated incorporating magneto-displacement effects using the multiscale modeling approach.

In Chapter 2, patterned multilayer Co/Ni microdisks were designed, fabricated, and tested for the bead capture application. Conventionally, the cell capture method has used an external magnetic field from permanent magnets or electromagnetic coils, which leads cells to aggregate to one location. This limits the space for cell imaging and analysis. Our proposed Co/Ni cell capture method demonstrates a way towards compact lab-on-a-chip devices for more precise control. In this work, finite element simulations were performed to assist the Co/Ni heterostructure design. A Co (0.2 nm)/Ni (0.4 nm) heterostructure was fabricated and tested in a suspension of fluorescent magnetic beads in a fluid. Magnetic beads were captured by the Co/Ni microdisks and mostly trapped at the perimeter of the disks, which agrees with the simulation results. Future studies need to be performed on releasing the magnetic beads with the designed materials structure of comparably small coercivity and the assistance of magnetoelectric effects.

In Chapter 3, magnetoelectric Co/Ni microdevices were fabricated on both Si and PMN-30PT(011) substrates to understand the roughness and magnetoelectric effects on the uniformity of magnetic response. We observed a non-uniform response on both Si and PMN-PT specimens. This further shows that inhomogeneous strain from PMN-PT substrate is not the primary cause of the observed dispersion. We observed a larger coercivity of Co/Ni disks on the PMN-PT than those on the Si substrate, which was attributed to the surface roughness effect. The strain-induced coercivity is modest when compared to the contributions from surface roughness and fabrication-induced imperfection. Anisotropy energy calculation was performed to explain the limited strain effect on the change of coercivity. Future design of strain modulated PMA based devices will require selection of material systems and processing techniques that lead to lower interfacial roughness, and improved edge/sidewall uniformity of microstructures, to realize a smaller coercivity for strain-induced coercive field modulation.

In Chapter 4, an atomic model was developed to understand static and dynamic magnetic behaviors using a multiscale modeling approach. A model of two Co adatoms residing on a Cu(100) substrate was studied incorporating the magneto-displacement effect. The parameters used in the phenomenological model were extracted from the DFT calculation. Coupled Newton's law and the LL equation governed the dynamics of the system. We observed an FM to AFM transition and change of eigenfrequencies of the system when increasing the distance between two Co adatoms. Moreover, displacement-assisted in-plane to out-of-plane switching was demonstrated. In the AFM case, the required external field to achieve IP to OOP switching significantly decreases from 64 T to 3 T. The outcome shows atomic level devices are promising for the potential application of quantum computing and storage devices. The future challenge of this atomic model is to expand from two to a large number of atoms. An approximation of the interactions between adatoms needs to be made to increase the calculation speed. Alternatively, molecular dynamics and other simulation methods can be implemented based on the results of this model for a large number of atoms.

This work covers fundamental studies and practical applications of multiferroics. Versatile multiferroics are an exciting and promising interdisciplinary research field. Practical multiferroic applications are very challenging. Extensive research efforts have been devoted to this field. I hope this work brings some inspiration to the readers.

References

[1] J. Cui *et al.*, "Generation of localized strain in a thin film piezoelectric to control individual magnetoelectric heterostructures," *Appl. Phys. Lett.*, vol. 107, no. 9, p. 092903, Aug. 2015.

[2] Y. Sun *et al.*, "Electric-Field Modulation of Interface Magnetic Anisotropy and Spin Reorientation Transition in (Co/Pt)3/PMN-PT Heterostructure," *ACS Appl. Mater. Interfaces*, vol. 9, no. 12, pp. 10855–10864, Mar. 2017.

[3] D. B. Gopman *et al.*, "Strain-assisted magnetization reversal in Co/Ni multilayers with perpendicular magnetic anisotropy," *Nat. Publ. Gr.*, vol. 6, no. 1, p. 27774, Sep. 2016.

[4] R. Sbiaa, H. Meng, and S. N. Piramanayagam, "Materials with perpendicular magnetic anisotropy for magnetic random access memory," *Phys. Status Solidi - Rapid Res. Lett.*, vol. 5, no. 12, pp. 413–419, Dec. 2011.

[5] G. Lu and E. Kaxiras, "Overview of Multiscale Simulations of Materials," 2005.

[6] S. Yamamoto and I. Matsuda, "Measurement of the Resonant Magneto-Optical Kerr Effect Using a Free Electron Laser," *Appl. Sci. 2017, Vol. 7, Page 662*, vol. 7, no. 7, p. 662, Jun. 2017.

[7] V. P. Antropov, M. I. Katsnelson, M. Van Schilfgaarde, and B. N. Harmon', "Ab Initio Spin Dynamics in Magnets," vol. 75, no. 4, 1995.

[8] S. Westmoreland *et al.*, "Multiscale model approaches to the design of advanced permanent magnets The microscopic mechanism for laser induced ultrafast demagnetization View project Micromagnetic energy minimization View project

Multiscale model approaches to the design of advanced permanent magnets.”

[9] G. Brown, M. A. Novotny, and P. A. Rikvold, “Langevin simulation of thermally activated magnetization reversal in nanoscale pillars,” *Phys. Rev. B*, vol. 64, no. 13, p. 134422, Sep. 2001.

[10] J. Eriksson, O., Bergman, A., Bergqvist, L., & Hellsvik, *Atomistic Spin Dynamics: Foundations and Applications*. Oxford university press., 2017.

[11] G. P. Müller *et al.*, “*Spirit*: Multifunctional framework for atomistic spin simulations,” *Phys. Rev. B*, vol. 99, no. 22, p. 224414, Jun. 2019.

[12] R. F. L. Evans, W. J. Fan, P. Chureemart, T. A. Ostler, M. O. A. Ellis, and R. W. Chantrell, “Atomistic spin model simulations of magnetic nanomaterials,” *J. Phys. Condens. Matter*, vol. 26, no. 10, p. 103202, 2014.

[13] U. Atxitia, P. Nieves, and O. Chubykalo-Fesenko, “Landau-Lifshitz-Bloch equation for ferrimagnetic materials,” *Phys. Rev. B*, vol. 86, 2012.

[14] B. Skubic, J. Hellsvik, L. Nordström, and O. Eriksson, “A method for atomistic spin dynamics simulations: implementation and examples,” *J. Phys. Condens. Matter J. Phys. Condens. Matter*, vol. 20, pp. 315203–12, 2008.

[15] J. D. Adams, U. Kim, and H. T. Soh, “Multitarget magnetic activated cell sorter.,” *Proc. Natl. Acad. Sci. U. S. A.*, vol. 105, no. 47, pp. 18165–70, Nov. 2008.

[16] S. Miltenyi, W. Müller, W. Weichel, and A. Radbruch, “High gradient magnetic cell separation with MACS,” *Cytometry*, vol. 11, no. 2, pp. 231–238, 1990.

[17] N. Pamme, “Magnetism and microfluidics,” *Lab Chip*, vol. 6, no. 1, pp. 24–38, Dec. 2006.

[18] F. J. A. J. A. Den Broeder, W. Hoving, and P. J. H. J. H. Bloemen, “Magnetic anisotropy of multilayers,” Feb. 1991.

[19] N. / Cu *et al.*, “Perpendicular magnetic anisotropy, domains, and misfit strain "Ni"/Cu/Si(001) thin films,” 1995.

[20] J.-M. L. Beaujour, W. Chen, K. Krycka, C.-C. Kao, J. Z. Sun, and A. D. Kent, “Ferromagnetic resonance study of sputtered Co|Ni multilayers,” *Eur. Phys. J. B*, vol. 59, pp. 475–483, 2007.

[21] M. T. Johnson, P. J. H. Bloemen, F. J. A. den Broeder, and J. J. de Vries, “Magnetic anisotropy in metallic multilayers,” *Reports Prog. Phys.*, vol. 59, no. 11, pp. 1409–1458, Nov. 1996.

[22] R. Sbiaa, H. Meng, and S. N. Piramanayagam, “Materials with perpendicular magnetic anisotropy for magnetic random access memory,” *Phys. status solidi - Rapid Res. Lett.*, vol. 5, no. 12, pp. 413–419, Dec. 2011.

[23] A. Hultgren, M. Tanase, C. S. Chen, G. J. Meyer, and D. H. Reich, “Cell manipulation using magnetic nanowires,” *Cit. J. Appl. Phys.*, vol. 93, p. 7554, 2003.

[24] H. Yun, K. Kim, and W. G. Lee, “Cell manipulation in microfluidics,” *Biofabrication*, vol. 5, no. 2, p. 022001, Feb. 2013.

[25] J. Voldman, “ELECTRICAL FORCES FOR MICROSCALE CELL MANIPULATION,” *Annu. Rev. Biomed. Eng.*, vol. 8, no. 1, pp. 425–454, Aug. 2006.

[26] A. Ashkin and J. M. Dziedzic, “Internal cell manipulation using infrared laser traps.,” *Proc. Natl. Acad. Sci. U. S. A.*, vol. 86, no. 20, pp. 7914–8, Oct. 1989.

[27] Y. Tokura, “Multiferroics—toward strong coupling between magnetization and polarization in a solid,” *J. Magn. Magn. Mater.*, vol. 310, no. 2, pp. 1145–1150, Mar. 2007.

[28] C. Liu, T. Stakenborg, S. Peeters, and L. Lagae, “Cell manipulation with magnetic particles toward microfluidic cytometry,” *J. Appl. Phys.*, vol. 105, no. 10, p. 102014, May 2009.

[29] G. Medoro, N. Manaresi, A. Leonardi, L. Altomare, M. Tartagni, and R. Guerrieri, “A lab-on-a-chip for cell detection and manipulation,” *IEEE Sens. J.*, vol. 3, no. 3, pp. 317–325, Jun. 2003.

[30] Z. Xiao *et al.*, “Cytocompatible magnetostrictive microstructures for nano- and microparticle manipulation on linear strain response piezoelectrics,” *Multifunct. Mater.*, vol. 1, no. 1, p. 014004, Nov. 2018.

[31] M. T. Johnson, J. H. Bloemen, J. A. Den Broeder, and J. J. De Vries, “Magnetic anisotropy in metallic multilayers,” 1996.

[32] C.-Y. Liang *et al.*, “Modeling of magnetoelastic nanostructures with a fully coupled mechanical-micromagnetic model,” *Nanotechnology*, vol. 25, no. 43, p. 435701, Oct. 2014.

[33] A. Barra, A. Mal, G. Carman, and A. Sepulveda, “Voltage induced mechanical/spin wave propagation over long distances,” *Appl. Phys. Lett.*, vol. 110, no. 7, p. 072401, Feb. 2017.

[34] Z. Xiao *et al.*, “Bi-directional coupling in strain-mediated multiferroic heterostructures with magnetic domains and domain wall motion,” *Sci. Rep.*, vol. 8, no. 1, p. 5207, Dec.

2018.

[35] E. A. Rapoport, "Magnetic domain walls for on-chip transport and detection of superparamagnetic beads," 2014.

[36] P. Chen, Y.-Y. Huang, K. Hoshino, and J. X. J. Zhang, "Microscale Magnetic Field Modulation for Enhanced Capture and Distribution of Rare Circulating Tumor Cells."

[37] J. P. Domann, C. Chen, A. E. Sepulveda, R. N. Candler, and G. P. Carman, "Multiferroic Micro-Motors with Deterministic Single Input Control," Feb. 2018.

[38] "The magnetization of pure iron and nickel," 1971.

[39] E. F. Kneller and R. Hawig, "The exchange-spring magnet: a new material principle for permanent magnets," *IEEE Trans. Magn.*, vol. 27, no. 4, pp. 3588–3560, Jul. 1991.

[40] C. Kittel, "On the Theory of Ferromagnetic Resonance Absorption," *Phys. Rev.*, vol. 73, no. 2, pp. 155–161, Jan. 1948.

[41] G. H. O. Daalderop, P. 3 Kelly, and A. Den Broeder, "Prediction and ConSrmation of Perpendicular Magnetic Anisotropy in Co/Ni Multilayers," 1992.

[42] S. Mangin, D. Ravelosona, J. A. Katine, M. J. Carey, B. D. Terris, and E. E. Fullerton, "Current-induced magnetization reversal in nanopillars with perpendicular anisotropy," *Nat. Mater.*, vol. 5, no. 3, pp. 210–215, Mar. 2006.

[43] M. Gottwald *et al.*, "Co/Ni(111) superlattices studied by microscopy, x-ray absorption, and *ab initio* calculations," *Phys. Rev. B*, vol. 86, no. 1, p. 014425, Jul. 2012.

[44] N. Nakajima *et al.*, "Perpendicular Magnetic Anisotropy Caused by Interfacial Hybridization via Enhanced Orbital Moment in Co / Pt Multilayers: Magnetic Circular

X-Ray Dichroism Study," *Phys. Rev. Lett.*, vol. 81, no. 23, pp. 5229–5232, Dec. 1998.

[45] J.-M. Hu, L.-Q. Chen, and C.-W. Nan, "Multiferroic Heterostructures Integrating Ferroelectric and Magnetic Materials," *Adv. Mater.*, vol. 28, no. 1, pp. 15–39, Jan. 2016.

[46] X. Li *et al.*, "Strain-mediated 180° perpendicular magnetization switching of a single domain multiferroic structure," *J. Appl. Phys.*, vol. 118, no. 1, p. 014101, Jul. 2015.

[47] Q. Wang *et al.*, "Strain-mediated 180° switching in CoFeB and Terfenol-D nanodots with perpendicular magnetic anisotropy," *Appl. Phys. Lett.*, vol. 110, no. 10, p. 102903, Mar. 2017.

[48] D. Kim, E. Rozhkova, I. Ulasov, S. Bader, T. R.-N. materials, and undefined 2010, "Biofunctionalized magnetic-vortex microdiscs for targeted cancer-cell destruction," *nature.com*.

[49] K. Y. Castillo-Torres, D. P. Arnold, and E. S. McLamore, "Rapid isolation of Escherichia coli from water samples using magnetic microdiscs," *Sensors Actuators, B Chem.*, vol. 291, pp. 58–66, Jul. 2019.

[50] T. N. Zamay *et al.*, "Noninvasive Microsurgery Using Aptamer-Functionalized Magnetic Microdisks for Tumor Cell Eradication," *Nucleic Acid Ther.*, vol. 27, no. 2, pp. 105–114, Apr. 2017.

[51] Y. C. Hsiao *et al.*, "Capturing magnetic bead-based arrays using perpendicular magnetic anisotropy," *Appl. Phys. Lett.*, vol. 115, no. 8, p. 082402, Aug. 2019.

[52] J. E. Lenz, "A Review of Magnetic Sensors," *Proc. IEEE*, vol. 78, no. 6, pp. 973–989, 1990.

[53] J.-M. Hu and C.-W. Nan, “Opportunities and challenges for magnetoelectric devices,” *APL Mater.*, vol. 7, no. 8, p. 080905, Aug. 2019.

[54] R. Lo Conte *et al.*, “Influence of Nonuniform Micron-Scale Strain Distributions on the Electrical Reorientation of Magnetic Microstructures in a Composite Multiferroic Heterostructure,” 2018.

[55] G. P. Zhao and X. L. Wang, “Nucleation, pinning, and coercivity in magnetic nanosystems: An analytical micromagnetic approach,” *Phys. Rev. B - Condens. Matter Mater. Phys.*, vol. 74, no. 1, p. 012409, Jul. 2006.

[56] M. T. Bryan, D. Atkinson, and R. P. Cowburn, “Edge roughness and coercivity in magnetic nanostructures,” *J. Phys. Conf. Ser.*, vol. 17, no. 1, p. 006, Jan. 2005.

[57] J. Qiu, Z. Meng, Y. Yang, J. F. Ying, Q. J. Yap, and G. Han, “Effect of roughness on perpendicular magnetic anisotropy in (Co90Fe10/Pt)n superlattices,” *AIP Adv.*, vol. 6, no. 5, p. 056123, May 2016.

[58] J. M. Shaw, H. T. Nembach, and T. J. Silva, “Roughness induced magnetic inhomogeneity in Co/Ni multilayers: Ferromagnetic resonance and switching properties in nanostructures,” *Cit. J. Appl. Phys.*, vol. 108, p. 93922, 2010.

[59] J. Kim and S. Shin, “Interface roughness effects on the surface anisotropy in Co/Pt multilayer films,” *J. Appl. Phys.*, vol. 80, no. 5, pp. 3121–3123, Sep. 1996.

[60] M. Arora, R. Hübner, D. Suess, B. Heinrich, and E. Girt, “Origin of perpendicular magnetic anisotropy in Co/Ni multilayers,” *Phys. Rev. B*, vol. 96, p. 24401, 2017.

[61] L. You, R. C. Sousa, S. Bandiera, B. Rodmacq, and B. Dieny, “Co/Ni multilayers with

perpendicular anisotropy for spintronic device applications," *Cit. Appl. Phys. Lett*, vol. 100, no. 17, p. 172411, Apr. 2012.

[62] D. B. Gopman *et al.*, "Large Interfacial Magnetostriction in (Co/Ni) 4 /Pb(Mg 1/3 Nb 2/3)O 3 − PbTiO 3 Multiferroic Heterostructures," 2018.

[63] "Certain commercial equipment, instruments, or materials are identified in this paper in order to specify the experimental procedure adequately. Such identification is not intended to imply recommendation or endorsement by NIST, nor is it intended to imply." .

[64] H. Kurt, M. Venkatesan, and J. M. D. Coey, "Enhanced perpendicular magnetic anisotropy in Co/Ni multilayers with a thin seed layer," *J. Appl. Phys.*, vol. 108, no. 7, p. 073916, Oct. 2010.

[65] V. Elshocht, A. Furnemont, J. De Boeck, and G. Kar, "Seed layer impact on structural and magnetic properties of [Co/Ni] multilayers with perpendicular magnetic anisotropy," *J. Appl. Phys*, vol. 121, p. 43905, 2017.

[66] C. A. Schneider, W. S. Rasband, and K. W. Eliceiri, "NIH Image to ImageJ: 25 years of image analysis," *Nat. Methods 2012 97*, vol. 9, no. 7, pp. 671–675, Jun. 2012.

[67] G. Palasantzas, Y. P. Zhao, J. T. M. De Hosson, and G. C. Wang, "Roughness effects on magnetic properties of thin films," *Phys. B Condens. Matter*, vol. 283, no. 1–3, pp. 199–202, Jun. 2000.

[68] Y. Sun *et al.*, "Electric-Field Modulation of Interface Magnetic Anisotropy and Spin Reorientation Transition in $(Co/Pt)_3$ /PMN–PT Heterostructure," *ACS Appl. Mater. Interfaces*, vol. 9, no. 12, pp. 10855–10864, Mar. 2017.

[69] K. Kyuno, J. -G. Ha, R. Yamamoto, and S. Asano, “Theoretical study on the strain dependence of the magnetic anisotropy of X/Co(X=Pt, Cu, Ag, and Au) metallic multilayers,” *J. Appl. Phys.*, vol. 79, no. 9, pp. 7084–7089, May 1996.

[70] A. Spinelli, B. Bryant, F. Delgado, J. Fernández-Rossier, and A. F. Otte, “Imaging of spin waves in atomically designed nanomagnets,” 2014.

[71] E. Prati, “Atomic scale nanoelectronics for quantum neuromorphic devices: Comparing different materials,” *Int. J. Nanotechnol.*, vol. 13, no. 7, pp. 509–523, 2016.

[72] M. Gündoğan, M. Mazzera, P. M. Ledingham, M. Cristiani, and H. de Riedmatten, “Coherent storage of temporally multimode light using a spin-wave atomic frequency comb memory,” *New J. Phys.*, vol. 15, no. 4, p. 045012, Apr. 2013.

[73] D. Afanasiev *et al.*, “Ultrafast control of magnetic interactions via light-driven phonons,” *Nat. Mater. 2021 205*, vol. 20, no. 5, pp. 607–611, Feb. 2021.

[74] G. Yahia *et al.*, “Recognition of exchange striction as the origin of magnetoelectric coupling in multiferroics,” *Phys. Rev. B*, vol. 95, no. 18, p. 184112, May 2017.

[75] E. Valiev *et al.*, “Application of the exchange-striction model for the calculation of the FeRh alloys magnetic properties,” *Intermetallics*, vol. 108, pp. 81–86, May 2019.

[76] R. L. Snyder, V. Q. Nguyen, and R V Ramanujan, “Design parameters for magneto-elastic soft actuators,” 2010.

[77] R.-C. Peng, J.-M. Hu, K. Momeni, J.-J. Wang, L.-Q. Chen, and C.-W. Nan, “Fast 180° magnetization switching in a strain-mediated multiferroic heterostructure driven by a voltage,” *Sci. Reports 2016 61*, vol. 6, no. 1, pp. 1–9, Jun. 2016.

[78] A. B. Smith and R. V Jones, “Magnetostriction Constants from Ferromagnetic Resonance ARTICLES YOU MAY BE INTERESTED IN,” *J. Appl. Phys.*, vol. 34, p. 1283, 1963.

[79] J. A. Jones and M. Mosca, “Implementation of a quantum algorithm on a nuclear magnetic resonance quantum computer,” *J. Chem. Phys*, vol. 109, p. 1648, 1998.

[80] P. Rabl, P. Cappellaro, M. V. G. Dutt, L. Jiang, J. R. Maze, and M. D. Lukin, “Strong magnetic coupling between an electronic spin qubit and a mechanical resonator.”

[81] I. Lovchinsky *et al.*, “Magnetic resonance spectroscopy of an atomically thin material using a single-spin qubit,” *Science (80-.).*, vol. 355, no. 6324, pp. 503–507, Feb. 2017.

[82] N. Knorr, M. A. Schneider, L. Diekhöner, P. Wahl, and K. Kern, “Kondo Effect of Single Co Adatoms on Cu Surfaces,” 2002.

[83] P. P. Baruselli, R. Requist, A. Smogunov, M. Fabrizio, and E. Tosatti, “Co adatoms on Cu surfaces: Ballistic conductance and Kondo temperature.”

[84] Q. L. Li *et al.*, “Role of the surface state in the Kondo resonance width of a Co single adatom on Ag(111),” *Phys. Rev. B*, vol. 97, no. 3, p. 035417, Jan. 2018.

[85] R. Skomski, “RKKY interactions between nanomagnets of arbitrary shape,” *Eur. Lett*, vol. 48, no. 4, pp. 455–460, 1999.

[86] J. A. Stroscio and R. J. Celotta, “Controlling the dynamics of a single atom in lateral atom manipulation,” *Science (80-.).*, vol. 306, no. 5694, pp. 242–247, Oct. 2004.

[87] D. Serrate *et al.*, “Imaging and manipulating the spin direction of individual atoms,” *Nat. Nanotechnol.* |, vol. 5, 2010.

[88] M. Lakshmanan, “The fascinating world of the LandauLifshitzGilbert equation: an

overview," *Philos. Trans. R. Soc. A Math. Phys. Eng. Sci.*, vol. 369, no. 1939, pp. 1280–1300, Mar. 2011.

[89] G. Kresse and J. Furthmüller, "Efficient iterative schemes for *ab initio* total-energy calculations using a plane-wave basis set," *Phys. Rev. B*, vol. 54, no. 16, p. 11169, Oct. 1996.

[90] G. Kresse and J. Furthmüller, "Efficiency of ab-initio total energy calculations for metals and semiconductors using a plane-wave basis set," *Comput. Mater. Sci.*, vol. 6, no. 1, pp. 15–50, Jul. 1996.

[91] J. P. Perdew, K. Burke, and M. Ernzerhof, "Generalized Gradient Approximation Made Simple," *Phys. Rev. Lett.*, vol. 77, no. 18, p. 3865, Oct. 1996.

[92] G. Kresse and D. Joubert, "From ultrasoft pseudopotentials to the projector augmented-wave method," *Phys. Rev. B*, vol. 59, no. 3, p. 1758, Jan. 1999.

[93] P. E. Blöchl, "Projector augmented-wave method," *Phys. Rev. B*, vol. 50, no. 24, p. 17953, Dec. 1994.

[94] D. M. Eigler and E. K. Schweizer, "Positioning single atoms with a scanning tunnelling microscope," *Nat. 1990 3446266*, vol. 344, no. 6266, pp. 524–526, 1990.

[95] P. Willke, K. Yang, Y. Bae, A. J. Heinrich, and C. P. Lutz, "Magnetic resonance imaging of single atoms on a surface," *Nat. Phys.*